A Connectomic Analysis of the Directional Selectivity Circuit in the Mouse Retina

by

Matthew Greene

B.A., Columbia University in the City of New York (2006)

Submitted to the Department of Brain and Cognitive Sciences
in partial fulfillment of the requirements for the degree of

Doctor of Philosophy

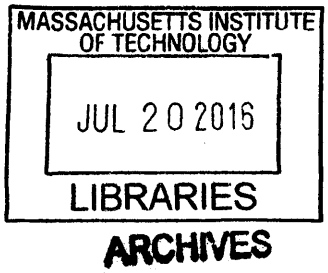

at the

MASSACHUSETTS INSTITUTE OF TECHNOLOGY

June 2016

Signature redacted

Author _____
Department of Brain and Cognitive Sciences
February 29, 2016

Signature redacted

Certified by _____
H Sebastian Seung
Professor of Brain and Cognitive Sciences
Thesis Supervisor

Signature redacted

Accepted by _____
Matthew A. Wilson
Sherman Fairchild Professor of Neuroscience and Picower Scholar
Director of Graduate Education for Brain and Cognitive Sciences

ABSTRACT. This thesis addresses the question of how direction selectivity (DS) arises in the mouse retina. DS has long been observed in retinal ganglion cells, and more recently confirmed in the starburst amacrine cell. Upstream retinal bipolar cells, however, have been shown to lac, indicating that the mechanism that gives rise to DS lies in the inner plexiform layer, where the axons of bipolar cells costratify with amacrine and ganglion cells.

We reconstructed a region of the IPL and identified cell types within it, and have discovered a mechanism which may explain the origin of DS activity in the mammalian retina, which relies on what we call "space-time wiring specificity." It has been suggested that a DS signal can arise from non-DS excitatory inputs if at least one among spatially segregated inputs transmits its signal with some delay, which we extend to consider also a difference in the degree to which the signal is sustained. Previously, it has been supposed that this delay occurs within the starburst amacrine cells' dendrites. We hypothesized an alternative, presynaptic mechanism. We observed that different bipolar cell types, which are believed to express different degrees of sustained activity, contact different regions of the starburst amacrine cell dendrite, giving rise to a space-time wiring specifity that should produce a DS signal. We additionally provide a model that predicts the strength of DS as a function of the spatial segregation of inputs and the temporal delay.

Contents

List of Figures 5
Acknowledgements 6

Chapter 1. Introduction 7
1.1. Retinal bipolar cells 7
1.2. Direction selectivity in retinal ganglion cells 8
1.3. The starburst amacrine cell 8
1.4. Existing Models of direction selectivity 9

Chapter 2. Reconstruction of the Retina by Man and Machine 13
2.1. Machine learning 13
2.2. Reconstruction by EyeWirers 13
2.3. Reconstruction by workers 16
2.4. BC Reconstruction 17
2.5. SAC reconstruction 18
2.6. Reconstruction Results 19
2.7. Aligning cells to a common coordinate system 19

Chapter 3. Classification of Bipolar Cells 23
3.1. Morphological classification of Bipolar Cells 23
3.2. Classification by Connectivity 28

Chapter 4. Direction Selectivity in the Off SAC 32
4.1. Contact analysis 32
4.2. Co-stratification analysis 33
4.3. Model of direction selectivity 37
4.4. Discussion 41

Chapter 5. Analagous Connectivity in the On SAC 44
5.1. BC-SAC contact analysis 45
5.2. BC-SAC co-stratification analysis 47
5.3. Discussion 48

Bibliography 51

List of Figures

1.1 The Starburst Amacrine Cell. 10
1.2 Hypothesized Models of Direction Selectivity 12

2.1 The value of resolution. 14
2.2 EyeWire combines crowd and artificial intelligence. 16
2.3 Overview of Off and On SAC. 20
2.4 Reconstructed volume. 21
2.5 Using SACs for volume alignment. 22

3.1 Off BC types 24
3.2 Off BC classification. 25
3.3 On BC classification. 27
3.4 Classification of On BC types. 29
3.5 Contact-based division of BC5. 31

4.1 BC-Off SAC contact. 34
4.2 Alternative contact analysis. 35
4.3 BC-SAC co-stratification. 36
4.4 Mathematical model of the BC-SAC circuit. 39
4.5 Model direction selectivity index (DSI) versus stimulus speed. 41

5.1 Organization of the inner plexiform layer 46
5.2 Robustness of Contact Analysis. 48
5.3 Wiring specificity of On BC-SAC circuit. 49

Acknowledgements

Firstly, I thank my adviser Sebastian Seung for giving me the opportunity to work and study at BCS. Sebastian has made everything in the past five years possible. I thank Sebastian also for having indirectly having introduced me to my wonderful wife Maria, whom I met in Sebastian's neural networks class.

The bulk of the work of this thesis is far greater than any one person could achieve, and in that regard, I thank colleague and serial co-author Jinseop Kim. Jinseop worked for many years curating the data and supervising the workers who made the reconstructions featured here possible. I wish Jinseop the best in all his future endeavors.

The reconstructions were created both by the crowdsourcing platform "EyeWire" and by professional tracers working alongside other lab members. I acknowledge the continuous effort of both the Eyewirers and all the professional reconstructors, and especially Rachel Prentki, who demonstrated that no resource is more necessary in the reconstruction of neural data than human intelligence.

I thank all the developers of the software that made the receonstruction effort possible. Foremost among these are Mark Richardson, Michael Purcaro, and Matt Balkamm, who all went far above and beyond the call of your average software engineers, squashing many bugs and ultimately producing a very slick product despite having a very small team

I thank all my other academic colleagues in the Seung lab for all the advice and comeraderie that was provided over the years. Viren Jain and Srinivas Turaga both taught me a great deal about neural networks and about the best pubs in Cambridge. My long-time office-mate Daniel Berger was always a source of interesting conversations and curious observations. Neville Sanjana and Jen Wang likewise were a delight to be around, and always reming me of some of the most fun times in the lab.

I separately thank labmates Aleks Zlateski, who is also my former roommate, Uygar Sumbul, and Ignacio Arganda-Carreras. In the latter couple of years, this trio was the heart of the lab. They were always full of interesting stories of late-night escapades with two of our other great friends, Ranko Sredojovic and Jovana Knezekic.

Lastly, I thank my incredible wife Maria, and our children Gambit and Vivian for their love and support. No academic accomplishment can match the joy my family brings me.

CHAPTER 1

Introduction

Compared to cognitive functions such as language, the visual detection of motion may seem trivial, yet the underlying neural mechanisms have remained elusive for half a century Borst and Euler [2011], Vaney et al. [2012]. Some retinal outputs (ganglion cells) respond selectively to visual stimuli moving in particular directions, while retinal inputs (photoreceptors) lack direction selectivity (DS). How does DS emerge from the microcircuitry connecting inputs to outputs?

DS has been observed in the starburst amacrine cell (SAC), and several types of directionally selective ganglion cells (DSGCs). It has been shown that the upstream source of excitation to these cells, which is provided by retinal bipolar cells (BCs) lacks DS [Yonehara et al., 2013]. Thus, the mechanism of DS arises somewhere in the region of the retina where these cells interact, the inner plexiform layer (IPL).

1.1. Retinal bipolar cells

Bipolar cells (BCs) provide the sole pathway from the photoreceptors of the retina to the amacrine and ganglion cells of the IPL. Since most amacrine cells (ACs) are inhibitory, and ganglion cells (GCs) do not synapse presynaptically within the IPL, BCs can be considered the primary source of excitatory input to the IPL.

Retinal bipolar cells were first subdivided into classes by the polarity of their central receptive field response (OFF or ON) [Werblin and Dowling, 1969, Kaneko, 1970] or by whether their synapses with photoreceptors were "flat" or "invaginating" [Missotten, 1965, Dowling and Boycott, 1966]. These classifications were initially thought to be related through observations in the cyprinid fish [Famiglietti et al., 1977], but it was soon discovered in amphibians that the relationship was not universal [Lasansky 1978]. Rodent work in the grey squirrel further cast doubt on the validity of the synaptic classification, as a class of BC in the squirrel retina was found to have both flat and invaginating synapses with cone photoreceptors [West, 1978].

Research in the late 1970s began to focus on classification using the depth of the stratification of the axonal arbor in the IPL [Famiglietti and Kolb, 1976b]. It was found that BCs with OFF centers stratify in the outer (proximal to the epithelium) region of the IPL, while BCs with ON centers stratify in the inner region. These outer and inner regions began to be referred to as subliminae a and b, respectively [Nelson et al., 1978]. The subdivision of BCs into more refined "types" demonstrates significant species difference. In the rabbit, it was observed through the reconstruction of individual neurons in electron micrograph images and through golgi staining that there existed at least nine distinct BC morphologies within the subliminae [Famiglietti, 1981, Mills and Massey, 1992]. Ghosh et al. [2004] extended this work to the mouse retina, wherein they identified nine cone BC types in addition to the rod BC using light microscopy with immunostaining to help distinguish cells

with different receptor types. This classification was further refined by Wässle et al. [2009] using additional immunocytochemical markers, revealing that Type 3 (BC3) as defined by Ghosh et al. [2004] consisted of two separate types, BC3a and BC3b. They also hypothesized that BC5 was in fact two cell types, which was later confirmed by Helmstaedter et al. [2013] through the dense reconstruction of electron micrograph images. Helmstaedter et al. [2013] also identified a BC type that co-stratifies with the other BC5s, but has a wider lateral span and stratifies more narrowly in IPL depth, and they further speculated that there may exist a third BC5 type.

The different types have been observed to have differing time lags in visual response. This is mostly characterized by a sustained verses transient response, rather than a latency difference [Baden et al., 2013, Borghuis et al., 2013]. While existing work has not yet conclusively determined which BC types show more sustained activity, evidence suggests that the IPL is subdivided not just into on and off regions, but that these sublamina are further subdivided into sustained and transient regions at the depths stratified by SACs.

1.2. Direction selectivity in retinal ganglion cells

Among the earliest work in the study of the behavior of cells in the vertibrate retina was that of Hartline in his 1938 account. There it was discovered that there exists at least three types of retinal ganglion cells (GCs) that respond to different stimulus features. He identified ON cells that would respond to the onset of a light stimulus, OFF cells that would respond to the termination of light stimulation, and ON-OFF cells that respond to both the onset and termination of light. These observations were followed in the 1950s and early 1960s by several researchers, who demonstrated that there were units responding to more complicated features, such as convexity, dimming, and color specificity [Lettvin et al., 1959, Wiesel, 1960, Wolbarsht et al., 1961]

Barlow et al. [1964] were the first to discover directionally selective (DS) GCs. They observed a class of GC that responds to both ON and OFF stimuli that moves in a specific direction. While On-Off DSGCs come in four subtypes, one for a preference in each of the four cardinal directions, other DSGCs in the mouse have been identified that don't have such diversity. The On DSGC can have one of three preferred directions, while Off DSGCs, such as the ventral-preferring JAMB-cell, have been found that only ever prefer a single direction [Kim et al., 2008].

1.3. The starburst amacrine cell

In the 1980s, the starburst amacrine cell (SAC), a neuronal cell type in the mammalian retina, was discovered and characterized [Famiglietti, 1983]. SAC dendrites receive excitatory input synapses from bipolar cells (BCs), which in turn receive input from photoreceptors. SAC dendrites also make synapses onto ganglion cells [Famiglietti, 1991], which send signals from the retina to the brain through the optic nerve. Like most other amacrine cells, SACs lack an axon; their output synapses are found in the distal zones of their dendrites.

There are two subtypes of SACs, one stratifying in the OFF sublayer of the IPL and one in the ON sublayer. The latter are sometimes called "displaced" SACs due to their somata appearing in the ganglion cell layer rather than the inner nuclear

layer. The two types are morphologically very similar, although OFF SACs tend to be about 15% larger than their ON counterparts.

Research on the question of directional selectivity has converged upon SAC. Borg-Graham and Grzywacz [1992] observed that SAC dendrites could function as temporal delay lines, as time is required for current from input synapses to propagate to output synapses (Fig. 1.2c). They modeled SAC dendrites as passive electrical cables, and showed that temporal delays could lead to direction selectivity, as had been observed more generally by Rall [1964]. Their passive cable model can be approximated by a Reichardt detector, if BC input synapses onto an SAC dendrite are lumped into two groups: (1) proximal synapses near the soma, and (2) distal synapses near the dendritic tips and the output synapses (Fig. 1.2c). Since proximal synapses are the delayed input and distal synapses the nondelayed input, Borg-Graham and Grzywacz [1992] predicted that outward motion should activate SAC dendrites more than inward motion.

Remarkably, their prediction of SAC direction selectivity was confirmed ten years later [Euler et al., 2002], as well as their prediction of an outward "preferred direction" (PD). A SAC dendrite is more activated by motion outward from the cell body to the tip of the dendrite, than by motion in the opposite direction [Euler et al., 2002]. Therefore a SAC dendrite exhibits DS, and outward motion is said to be its "preferred direction." Note that it is incorrect to assign a single such direction to a SAC, because each of the cell's dendrites has its own preferred direction (Fig. 1.1a). DS persists after blocking inhibitory synaptic transmission [Hausselt et al., 2007], when the only remaining inputs to SACs are bipolar cells (BCs), which are excitatory. Since the SAC exhibits DS, while its BC inputs do not [Yonehara et al., 2013], we say that DS *emerges* from the BC-SAC circuit. More recently, it was shown that BC inputs do not exhibit direction selectivity [Yonehara et al., 2013], confirming their assumption that motion detection occurs somewhere between BCs and SACs.

However, an inconsistency with empirical data also emerged. According to the model, the soma should depolarize more for inward motion than for outward motion, i.e., have a PD opposite that of the distal dendrites (Fig. 1.2e). In fact, the PDs of the soma and distal zone turn out to be the same [Euler et al., 2002]. To resolve this inconsistency, Hausselt et al. [2007] argued that active conductances must be added to the passive cable model of the SAC dendrite.

Inhibitory connections between SACs are also known to exist [Lee and Zhou, 2006], and can contribute to SAC direction selectivity [Zhou and Lee, 2008]. However, SAC-SAC inhibition does not appear necessary for direction selectivity, which persists even during pharmacological blockade of inhibitory synaptic transmission [Hausselt et al., 2007]. Therefore the present work focuses on BC-SAC circuitry.

1.4. Existing Models of direction selectivity

When Barlow and Hill [1963] first direction selective ganglion cells, they believed that DS arose in these cells through lateral inhibition displaced toward the preferred direction. If inhibition passes through a temporal delay line, or the inhibitory signal is sustained for a longer duration than the excitatory signal, this displacement could yield DS responses (Fig. 1.2b). Wyatt and Daw [1975] further

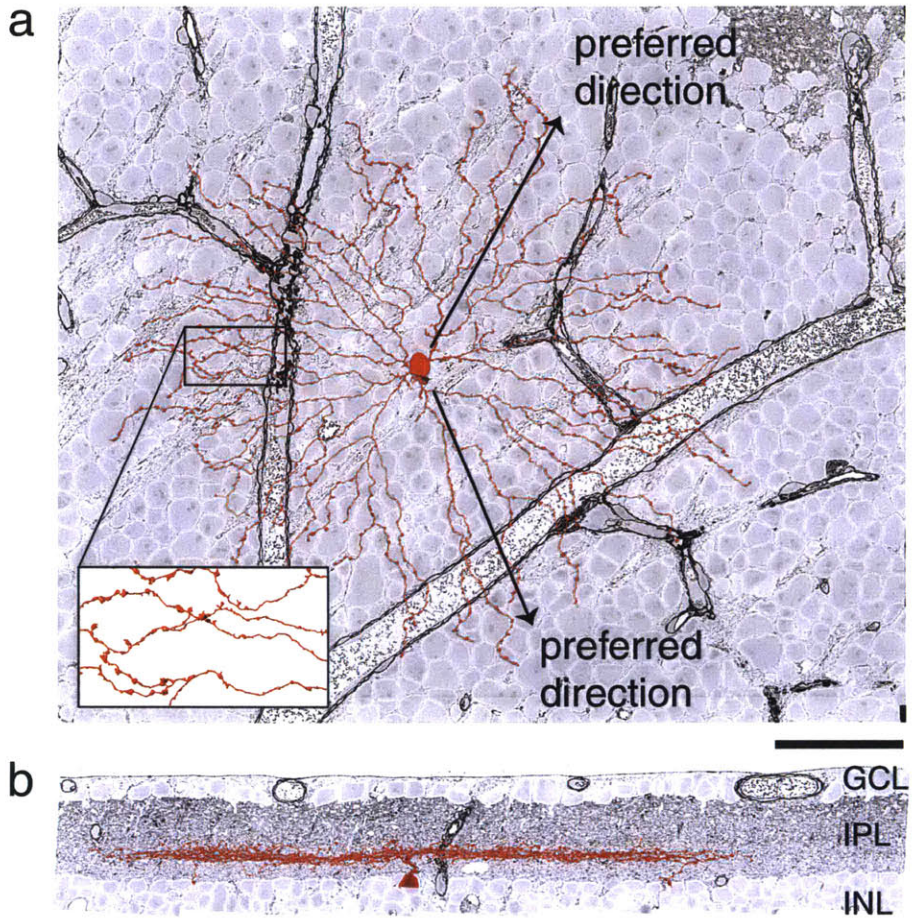

FIGURE 1.1. The Starburst Amacrine Cell.
An Off SAC. **a**, View of an SAC on the plane perpindicular to the light axis. Each dendrite of the SAC has a separate preferred direction oriented outward from the soma. The inset shows vericosities in the distal regions of the dendrite, indicating likely presynaptic sites. **b**, A view of the same SAC from a plane parallel to the light axis.

investigated this theory and confirmed the hypothesis. They identified a cardioid-shaped inhibitory receptive field around each point of excitation on the DSGC, biased in the preferred direction.

Another model exists that has appeared in models of biological motion detection since the 1950s, but has not previously been ascribed to a specific neural circuit in the mammalian visual system. Motion can be detected by correlating excitatory input signals from two locations, if one signal passes through a temporal delay line. Stimulation of the delayed input followed by the nondelayed input causes signals to arrive synchronously at the output element, and to activate it. Stimulation in

the opposite order gives rise to asynchronous signals at the output element, and no activation. In honor of the pioneering researcher Werner Reichardt, we will refer to the computational motif of Fig. 1.2a as a "Reichardt detector," although it is actually a subunit of his model [Reichardt, 1961].

The passive cable model of SAC direction selectivity is based on the assumption that the temporal delay in the Reichardt detector is due to propagation of signals within the SAC dendrites (Fig. 1.2d). This thesis explores another possibility: perhaps temporal delay could arise from mechanisms *presynaptic* to SAC dendrites (Fig. 1.2c), since mouse BCs have been classified into multiple types [Wässle et al., 2009], which are known to have distinct temporal behaviors [Baden et al., 2013, Borghuis et al., 2013]. If the connectivity of BC types with SACs varied with distance from the SAC soma, the BC-SAC circuit could end up resembling Fig. 1.2c. We tested this hypothesis by reconstructing BC-SAC circuitry using e2198, a dataset of mouse retinal images from serial block-face scanning electron microscopy (SBEM) [Briggman et al., 2011].

Motion is a spatiotemporal phenomenon: an object at one location appears somewhere else after a time delay. Therefore we wondered whether DS might arise because different locations on the SAC dendrite are wired to BC types with different time lags. More specifically, we hypothesized that the proximal BCs (wired near the SAC soma) lag the distal BCs (wired far from the soma).

Such "space-time wiring specificity" could lead to DS as follows (Fig. 1.2c). Motion outward from the soma will activate the proximal BCs followed by the distal BCs. If the stimulus speed is appropriate for the time lag, signals from both BC groups will reach the SAC dendrite simultaneously, summing to produce a large depolarization. For motion inward towards the soma, BC signals will reach the SAC dendrite asynchronously, causing only small depolarizations. Therefore the dendrite will "prefer" outward motion, as observed experimentally [Euler et al., 2002].

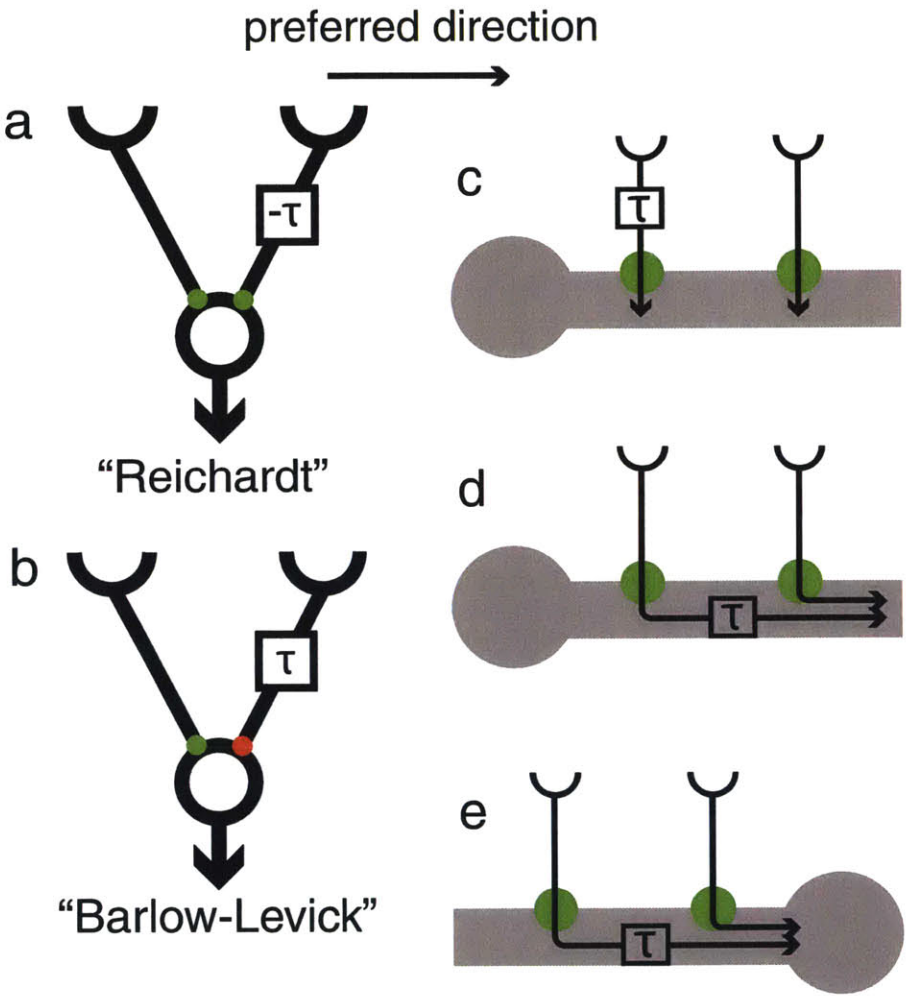

FIGURE 1.2. Hypothesized Models of Direction Selectivity
General and SAC-specific models of DS. **a**, A schematic representation of the Reichardt model. The two arms represent two spatially distinct excitatory inputs, with the input of the left arm being delayed relative to the right arm. If the detector is active only when it receives two simultaneous inputs, a stimulus moving from left to right in time τ will activate the detector, while a stimulus moving in the opposite direction will not. **b**, Similarly, the Barlow-Levick model has two arms with a delay line, but in this model, the delay is on the right arm, which provides inhibitory input rather than excitatory. If the detector is active only when it receives excitation without simultaneously receiving inhibition, once again only the rightward traveling stimulus will active the detector. **c**, A Reichardt-like mechanism for DS in the SAC, with the delay line occuring presynaptically [Tukker et al., 2004]. **d**, The same model, but with a postsynaptic delay line via intracellular signal propagation. **e**, An illustration of the observation that if there is a delay occuring through signal propagation, a stimulus traveling in the null direction should cause substantial depolarization in the soma, contrary to empirical observations [Euler et al., 2002].

CHAPTER 2

Reconstruction of the Retina by Man and Machine

30 years ago, John Graham White, under the supervision of Sydney Brenner, undertook the heroic task of reconstructing the connectome of a tiny worm known as caenorhabditis elegans[White et al., 1986]. He recognized that only electron micrography offered the resolution necessary to positively identify synaptic contacts, as demonstrated in Fig. 2.1. After a decade of labor, White produced the first connectome through almost entirely manual reconstruction. In some case, neural processes were even printed, and physical reconstructions were created as a means of visualization.

Happily, the development of modern computers allows us to substantially improve upon the reconstruction rate of White et al. We reconstructed e2198, an existing dataset of mouse retinal images from serial block-face scanning electron microscopy (SBEM) [Briggman et al., 2011]. The size of the data is approximately 350 μm x 350 μm x 50 μm, with the final dimension being parallel to the light axis. e2198 is located in the ventral portion of the retinal at a depth such that it spans the IPL and includes a portion of the INL and GCL.

2.1. Machine learning

The boundaries between neurons in subvolumes of the e2198 and e2006 datasets were manually traced by an expert. Using this as ground truth, a convolutional network (CN) was trained to detect boundaries between neurons using the MALIS method [Turaga et al., 2009]. The CN had the same architecture as one used previously [Helmstaedter et al., 2013], and produced as output an affinity graph connecting nearest neighbor voxels [Turaga et al., 2010]. Any subvolume of e2198 could be oversegmented by applying a modified watershed algorithm to the appropriate subgraph. The regions of the oversegmentation will be called supervoxels.

The e2198 dataset was oversegmented by an artificial intelligence (AI) into groups of neighboring voxels that were subsets of individual neurons. These "supervoxels" were assembled by humans into accurate 3D reconstructions of neurons.

2.2. Reconstruction by EyeWirers

In order to assemble the supervoxels produced by automatic segmentation, we primarily mobilized volunteers through EyeWire, a web site that turns 3D reconstruction of neurons into a game of coloring serial EM images.

Even before the learning in normal gameplay illustrated by Fig. 2.2a, all EyeWirers are required to go through a training session immediately after registering for the site. This consists of a sequence of tutorial cubes, each of which was previously colored by an expert . Each cube teaches through instructions and per-click feedback about accuracy based on comparing the EyeWirer's selections with those

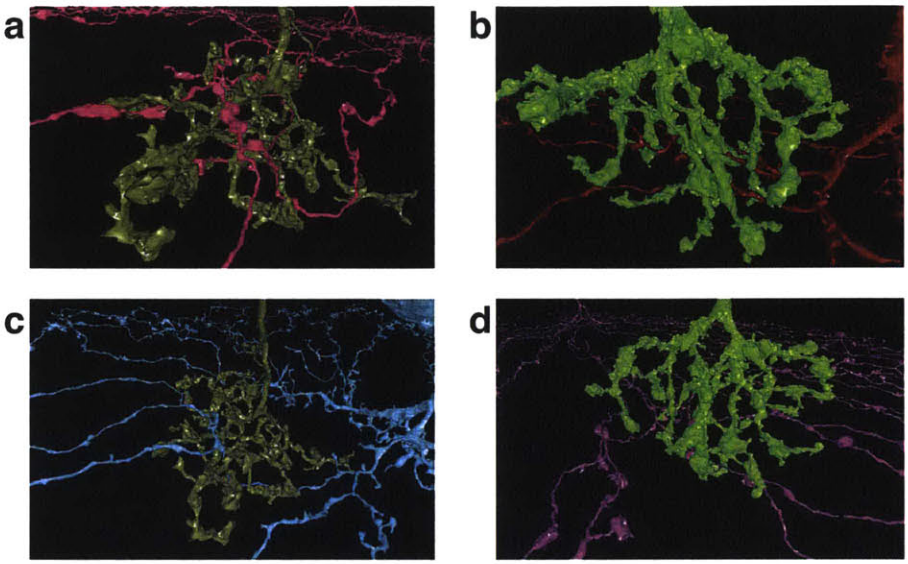

FIGURE 2.1. The value of resolution.
Each panel shows a bipolar cell and a starburst amacrine cell. The cells in **a** and **b** have significant contact, while those in **c** and **d** have no contact at all. It would be impossible to distinguish the two cases with the resolution offered by light microscopy.

of the expert. After submitting a tutorial cube, the EyeWirer is given a chance to view mistakes.

Accuracy is monitored on a weekly basis by computing the precision and recall of each EyeWirer with respect to the truth, defined as neuron reconstructions based on EyeWire consensus followed by GrimReaper corrections (Fig. 2.2c). Less accurate EyeWirers are given less weight in the vote, which appears to improve the overall accuracy of the system.

Players' daily, weekly, and monthly scores are publicly displayed on a leaderboard, motivating players to excel through competition. Players communicate with each other through online "chat" and discussion forums.

A "beta test" version of EyeWire was deployed in February 2012, and attracted a small group of users, who helped guide software development. After the official launch in December 2012, EyeWire was successful at reconstructing ganglion cells, but did not work well for reconstructing the more difficult SACs. In March 2013, EyeWirers were invited to the "Starburst Challenge," a sequence of tutorial cubes drawn from SACs. Those who passed with sufficient accuracy were an elite group allowed to reconstruct SACs (Supplementary Information).

Through EyeWire, we wanted to enable anyone, anywhere, to participate in our research. The approach is potentially scalable to extremely large numbers of "citizen scientists" [Lintott et al., 2008]. More importantly, the 3D reconstruction of neurons requires highly developed visuospatial abilities, and we wondered whether

a game could be more effective [Cooper et al., 2010] than traditional methods of recruiting and creating experts.

In gameplay mode, EyeWire shows a 2D slice through a "cube," an e2198 subvolume of 256^3 grayscale voxels (Fig. 2.2a). Gameplay consists of two activities: coloring the image near some location, or searching for a new location to color. Coloring is done by clicking at any location in the 2D slice, which causes the supervoxel containing that location to turn blue. Searching is done by translating and orienting the slice within the cube, and interacting with a 3D rendering of the colored supervoxels.

When the player first receives a cube, it already comes with a "seed," a contiguous set of colored supervoxels. The challenge is to color all the rest of the supervoxels that belong to the same neuron, and avoid coloring other neurons. Gameplay for a cube terminates when the player clicks "Submit," receives a numerical score, and proceeds to the next cube. Because our AI is sufficiently accurate, coloring supervoxels is faster than manually coloring voxels, an older approach to 3D reconstruction [Fiala, 2005].

The scoring system is designed to reward accurate coloring. This is nontrivial because EyeWire does not know the correct coloring. Each cube is assigned to multiple players (typically 5 to 10), and high scores are earned by players who color supervoxels that other players also color. In other words, the scoring system rewards agreement between players, which tends to be the same as rewarding accuracy.

Consensus is used not only to incentivize individual players, but also to enhance the accuracy of the entire system. Any player's coloring is equivalent to a set of supervoxels. Given the colorings of multiple players starting from the same seed in the same cube, a consensus can be computed by voting on each supervoxel. EyeWirer consensus was much more accurate than any individual EyeWirer (Fig. 2.2b,c). It remains possible that the consensus reconstructions contain inaccuracies, but such inaccuracies must be very small relative to the size of the entire cell, as large inaccuracies are extremely obvious to experts. This is because large mergers cause different regions of the "cell" to appear radically different, while large splits lead to clearly incomplete cells. More modest splits are possible, but provided they are rare and there is no notable bias in their location within a cellular arbor, the omission will not qualitatively influence analyses.

Coloring a neuron is more challenging than it sounds. Images are corrupted by noise and other artifacts. Neurites take paths that are difficult to predict, and can branch without warning. Careless errors result from lapses in attention. Extensive practice is required to achieve accuracy. The most accurate EyeWirers (Fig. 2.2c, upper right corner) often had experience with thousands of cubes. Improvements in accuracy were observed over the course of hundreds of cubes, corresponding to tens of hours of practice (Fig. 2.2d). According to subjective reports of EyeWirers, learning continues for much longer than that. In contrast, previous successes at "crowdsourcing" image analysis involved tasks that did not require such extensive training [Von Ahn and Dabbish, 2004, Lintott et al., 2008].

Reconstructing an entire neuron requires tracing its branches through thousands of cubes. This process is coordinated by an automatic spawner, which inspects each consensus cube for branches that exit the cube. Each exit generates a new cube and seed, which are added to a queue. EyeWirers are automatically

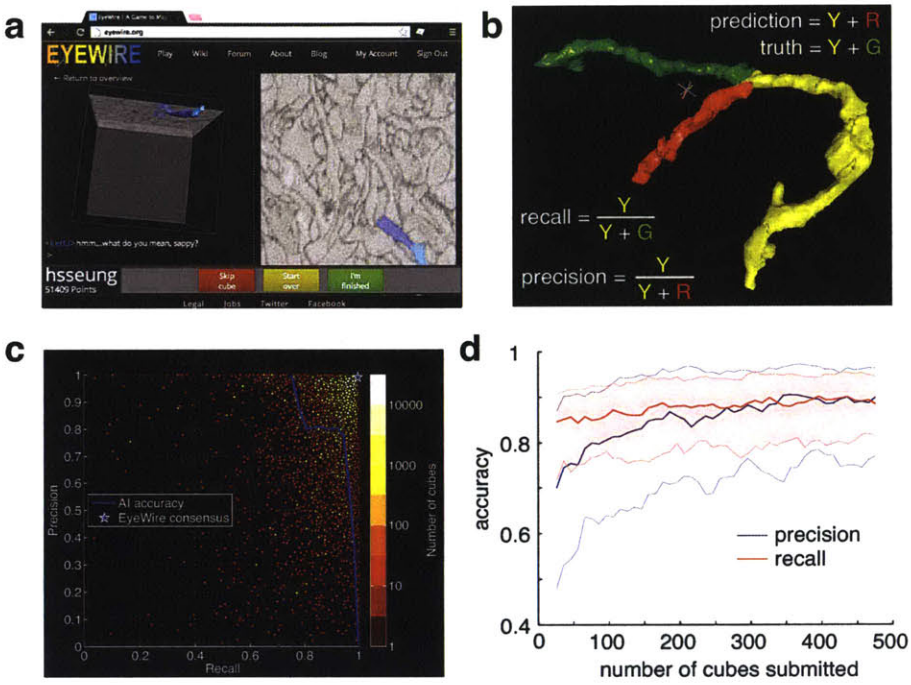

FIGURE 2.2. EyeWire combines crowd and artificial intelligence.

a, 3D and 2D views in the neuron reconstruction game. **b**, Precision and recall are two measures of accuracy. **c**, Accuracy of artificial intelligence (AI), 5881 EyeWirers, and EyeWirer consensus on reconstruction of a ganglion cell. **d**, EyeWirer precision and recall increase with number of cubes submitted. Solid lines are median values across 208 EyeWirers who submitted at least 500 cubes, and shaded regions indicate 25th to 75th percentile.

assigned to cubes by an algorithm that attempts to balance the number of plays for each cube.

Over 100,000 registered EyeWirers have been recruited by news reports, social media, and the EyeWire blog. Players span a broad range of ages and educational levels, come from over 130 countries, and the great majority have no formal training in neuroscience . These statistics show that EyeWire indeed widens participation in neuroscience research. At the same time, the most avid players constitute an elite group with disproportionate achievements. For example, the top 100 players have contributed about half of all cubes completed in EyeWire.

2.3. Reconstruction by workers

Lab workers also reconstructed neurons independently of EyeWire, with a more sophisticated version of the user interface developed in the lab called OMNI. Their

reconstructions were pooled with those of EyeWirers for the analyses reported below. Reconstruction error was quantified, and was treated like other kinds of experimental error when calculating confidence intervals from our data.

Workers were hired based on an interview and a short test of software use passed by 3/4 of the applicants. They were trained for 40 to 50 hours before generating reconstructions used for research. Their skills typically improved for months or even years after the initial training period, and were superior to those of professional neuroscientists without reconstruction experience.

As with EyeWire, the task of reconstructing an entire neuron was divided into subtasks, each of which involved reconstructing the neuron within a subvolume starting from a supervoxel "seed." However, the subvolumes were roughly 100 times larger than EyeWire cubes, and only two workers were assigned to each subvolume. In the first stage of error correction, disagreements were detected by computer, and resolved by one of the two workers, or a third worker. The third occasionally detected and corrected errors that were not disagreements between the first two. Most disagreements were the result of careless errors, and were easily resolved. More rarely, there were disagreements caused by fundamental ambiguities in the image. These locations were noted for later examination with more contextual information, as described below.

In the second stage of error correction, 3D reconstructions of entire neurons were assembled from multiple subvolumes and inspected. Experts visually detected suspicious branches or terminations, as well as overlaps between reconstructions of different neurons. The original image was reexamined at these locations to check for errors. The process was repeated until no further errors could be detected. The F-score (Fig. 2.2b) between the reconstructions before and after the second stage was 0.99 for SACs and 0.98 for BCs. Some errors may still remain, but it is likely that correcting them would have similarly little effect.

2.4. BC Reconstruction

Off BCs. Because only part of the inner nuclear layer (INL) was encompassed in e2198, the somata of Off bipolar cells (BCs) were generally outside the dataset. Therefore we searched the INL for candidate BC axons traveling between the somata, and traced them into the INL. Those that arborized in the Off region of the INL were further reconstructed. Cells that violated known BC structures were identified as amacrine cells and discarded [Helmstaedter et al., 2013].

BC axons were difficult to reconstruct due to poor staining, and their highly irregular shapes. They could not be accurately reconstructed (either by online volunteers or lab experts) within the 256^3 cubes of EyeWire, which were too small to provide sufficient spatial context. Therefore BCs were reconstructed only by lab workers using the large subvolumes mentioned above.

On BCs. On BCs were reconstructed mostly during February to December 2014. Because e2198 extends only partially into the INL, it was not possible to identify BCs based on the existence of a dendritic arbor in the OPL. Instead, we identified BC axonal arbors by comparison with Helmstaedter et al. [2013], who reconstructed all BCs in a patch of retina that included both IPL and OPL. BC axon candidates were neurites that pass through the interstices of the INL and emerge in the IPL. Many candidates could be immediately rejected as amacrine or ganglion cells because their arbors were too large, or rejected as glial cells based

on surface concavity and roughness. Little human effort was necessary for these cases, because large parts of these cells were automatically reconstructed. The remaining candidates were put into the reconstruction pipeline, and were rejected as narrow field amacrine cells if their stratification profiles deviated markedly from those previously reported by Helmstaedter et al. [2013] for BCs. Eight were rejected in the middle of reconstruction, and three were rejected after full reconstruction.

2.5. SAC reconstruction

Off SACs. Off SACs were reconstructed by (1) forward tracing from the soma to dendritic tips and (2) backward tracing from varicosities on candidate SAC dendrites to the soma. In the forward method, a candidate SAC soma was identified as a supervoxel with a characteristic pattern of dendritic stubs bearing spiny protrusions. By the time reconstruction progressed to approximately half of the average SAC radius, an Off SAC could be conclusively recognized by its starburst shape and narrow stratification at the appropriate IPL depth. More than 90% of candidates turned out to be SACs.

In the backward method, we located a thin dendrite with varicosities at the appropriate IPL depth. This was reconstructed back to the soma, and then the rest of the dendrites were reconstructed from the soma to the tips. The cell could be discarded at any point during this process, if its dendrites escaped from the appropriate IPL depth or failed to exhibit the proper morphological characteristics. Less than 25% of initial candidates ended up confirmed as SACs.

In total, 79 Off SACs were reconstructed, 39 by forward tracing and 52 by backward tracing. After candidates were identified by one of the authors (J.S.K.), reconstructions were performed by lab workers (59 cells) or by EyeWirers (29 cells). Overlapping numbers (12 for forward/backward, 9 for workers/EyeWirers) mean the combination of the two.

On SACs. On SACs were reconstructed mostly during July 2013 to September 2014. EyeWirers who helped reconstruct On SACs are listed in the Supplemental Information.

The forward-tracing method of identification turned out to be less useful for On SACs because their dendrites can take rather circuitous paths before reaching their final IPL depth and making the distinctive starburst shape. Therefore it takes a great deal of reconstruction effort before a candidate cell can be accepted or rejected as a SAC. It saves human effort if this decision can be made earlier in the reconstruction process. Two On SACs were reconstructed by lab workers using the forward method. The remaining 75 were reconstructed by EyeWirers using the backward method.

In a parallel study to be reported elsewhere, we exhaustively reconstructed all neurons with somata in a $(200\ \mu\text{m})^2$ GCL patch of e2198. This revealed 6 extra On SACs beyond the 35 in the patch that had already been reconstructed for the present study. In other words, the reconstructions of the present study had achieved 85% coverage of all On SACs in this $(200\ \mu\text{m})^2$ patch. Assuming that the density of On SACs is the same for all of e2198 as it is in the $(200\ \mu\text{m})^2$ patch, the estimated number of On SACs in e2198 is roughly 110, and our overall coverage is roughly 70%. Our estimated coverage of Off SACs is slightly lower, as the Off SAC density is known to be slightly (less than 10%) larger than the On SAC density [Jeon et al., 1998].

2.6. Reconstruction Results

The cell bodies of On and Off SACs are in the GCL and INL respectively, on opposite sides of the IPL (Fig. 5.1b, d). The reconstructions include 156 SACs (77 On and 79 Off, Fig. 5.1e), which we estimate is more than half of the SACs in e2198 (Experimental Procedures). The diameter of the SAC arbor is much larger than the spacing between cell bodies (Fig. 5.1e), so the arbors of adjacent SACs are highly overlapping. The reconstructions also include 271 On BC axons, coming close to complete coverage of all BCs in a subregion of e2198 roughly (0.1 mm)^2 in area (Fig. 5.1e). BC axons are much smaller than SAC arbors (Fig. 5.1e). The reconstructions of On SACs and BCs are new, while the Off SACs were reconstructed for a previous publication [Kim et al., 2014].

Length of SAC dendrites (Fig. 2.3 inset) was calculated as the mean distance from the soma on the xy plane of the eight most distant points that are not within 30 μm of each other. These parameters were chosen because the points generated appeared to give an accurate representation of the dendritic length, while avoiding inaccuracy that arises from outliers and from dendrites that extend beyond the bounds of the volume.

2.7. Aligning cells to a common coordinate system

For more precise quantification of structural properties, a new coordinate system was defined by applying a nonlinear transformation to reconstructed neurons so as to flatten the IPL and make it perpendicular to one of the coordinate axes. The nonlinear transformation was found by the following steps. First a global planar approximation to the Off SAC surface was computed. Then the centroid of all the SACs was projected onto this global plane to define the origin of the coordinate system. The projection was along the coordinate axis of the e2198 volume closest in direction to the light axis.

For analyses of the Off SAC, in order to correct for curvature, an azimuthal equidistant projection of the Off SAC surface onto the global plane was made about the origin . Then local planar approximations to the SAC surface were computed in the neighborhoods of every node in a triangular lattice. At each point in a triangle, the SAC surface was approximated by computing the mean of the planar approximations (as quaternions with yaw constrained to be zero) for the triangle's vertices, weighted by distance of the point from the vertices.

The Off SACs were defined as 32% IPL depth. We also reconstructed a few On SACs, and defined them as 62%. These choices placed the edge of the INL at 0%. Structural properties of all cells were computed based on the locations of their surface voxels after transformation into the new coordinates. All dimensions are uncorrected for tissue shrinkage, which was previously estimated at 14% by comparison of two-photon and serial EM images [Helmstaedter et al., 2013].

In analyses of On SACs, we improved the coordinate system by additionally utilizing On SACs as landmarks.

The volume was first rigidly transformed to minimize the averaged squared distance of Off SACs to the xy plane. A rectangular 32×36 lattice was defined on the xy plane, with nodes spaced at approximately 10 μm intervals. For each lattice node, we computed the mean depth of all Off SAC surface voxels and the mean depth of all On SAC surface voxels within a cylindrical neighborhood. Bilinear interpolation of these depths yielded values $\mu_{x,y}^{OFF}$ and $\mu_{x,y}^{ON}$ for every point in the

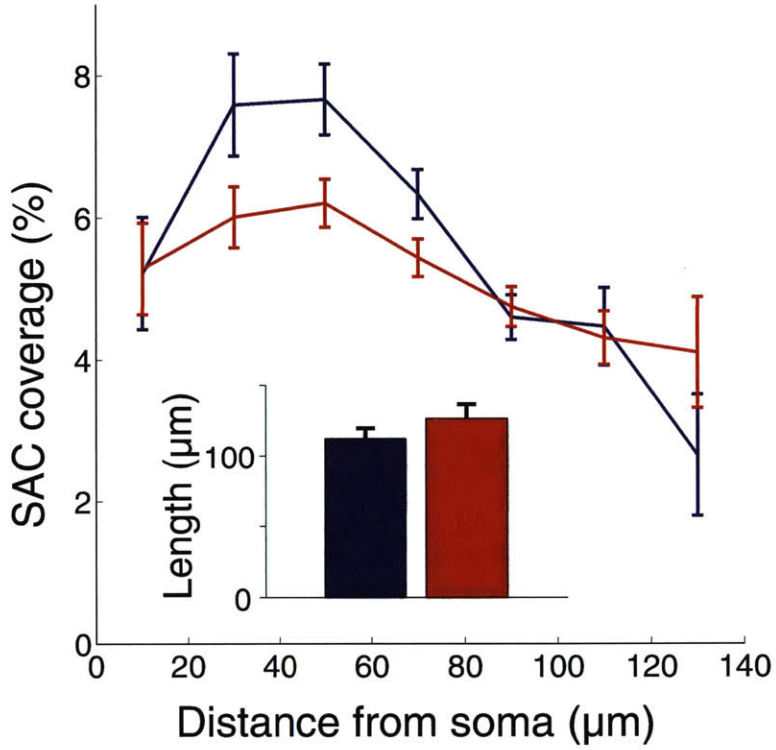

FIGURE 2.3. Overview of Off and On SAC.
Overview of properties of reconstructed On (blue) and Off (red) SACs. Plotted is the mean estimated percent of SAC surface area covered by BC contacts as a function of distance from the SAC soma. Inset is mean radius of reconstructed SAC, with error bars indicating standard error.

xy plane. Then the depth z of every point (x, y, z) was transformed according to $z' = \left(z - \mu_{x,y}^{OFF}\right) / \left(\mu_{x,y}^{ON} - \mu_{x,y}^{OFF}\right)$, yielding a coordinate system in which Off and On SACs are at depths 0 and 1, respectively. Finally we linearly transformed to coordinates in which Off and On SACs are at 0.28 and 0.62 IPL depth, respectively, for consistency with the definitions of Helmstaedter et al. [2013].

\It is standard to use On and Off SACs as landmarks to define IPL depth. Since the IPL has curvature and variations in thickness (Fig. 2.5a), we computationally flattened the retina by transforming the On and Off SACs into parallel planes (Fig. 2.5b). This type of coordinate transformation improves the accuracy of stratification profiles, and has previously been applied in light microscopic anatomy [Manookin et al., 2008, Siegert et al., 2009, Sümbül et al., 2014]. Average On and Off SAC stratification profiles became narrower after the transformation (Fig. 2.5c).

Famiglietti [1983] divided SAC dendrites into proximal, intermediate, and distal zones. The median stratification depth of SAC dendrites varies strongly in the

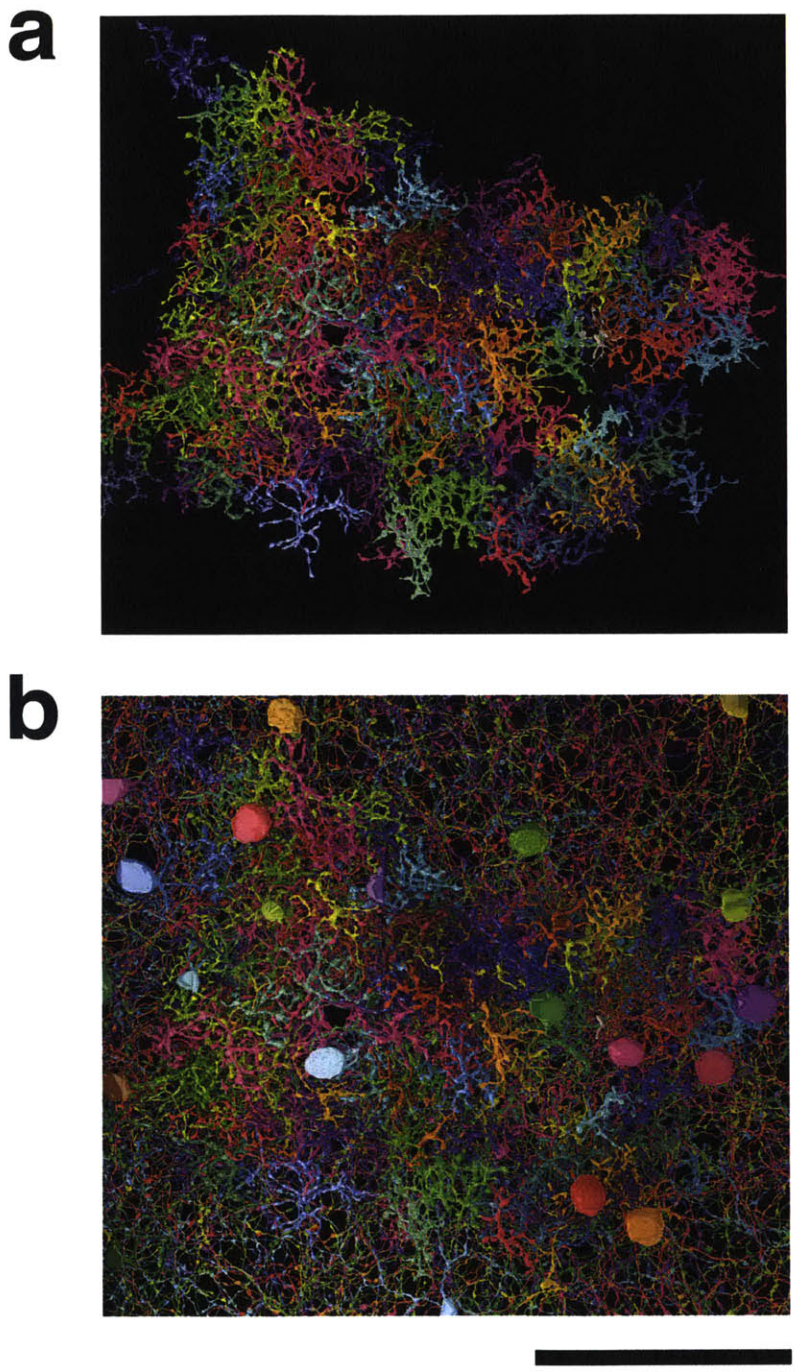

FIGURE 2.4. Reconstructed volume.
a, Rendering of reconstructed off BCs. **b**, Rendering of reconstructed off starburst amacrine cells and off BCs. Scale bar is $50\mu m$

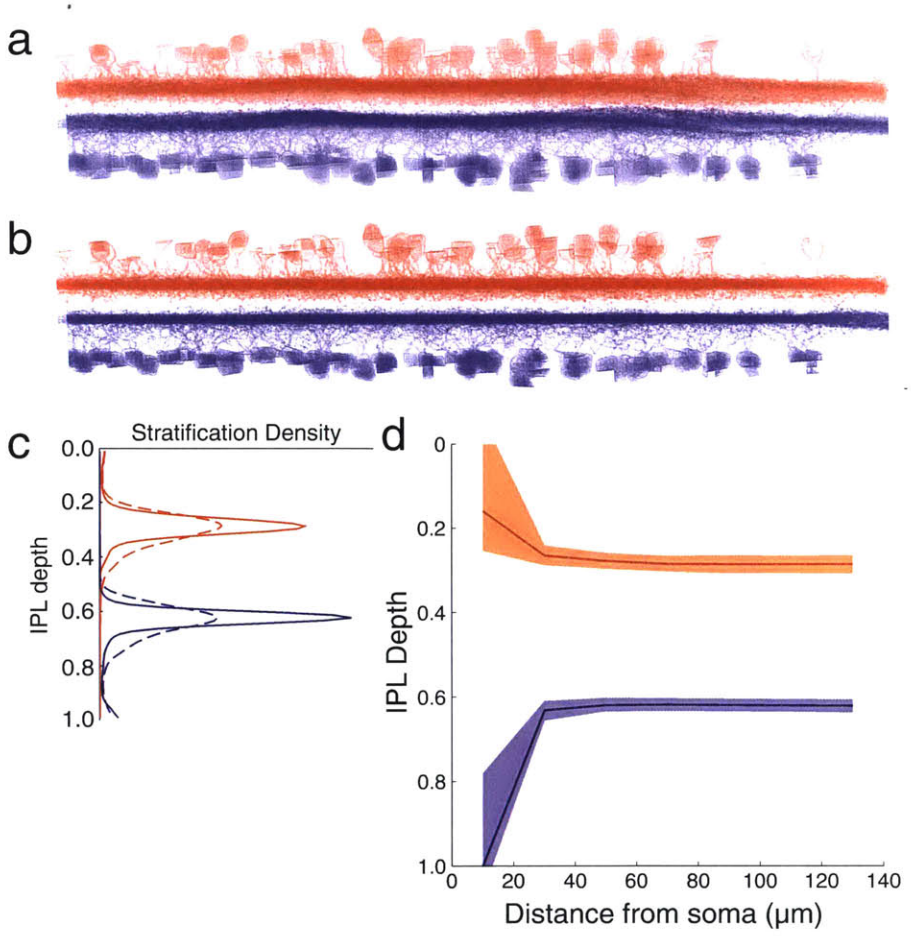

FIGURE 2.5. Using SACs for volume alignment.
On (blue) and Off (red) SACs and their usage as landmarks for quantifying IPL depth. **a,** SACs projected along a tangential axis, after rigid alignment to the tangential plane. Curvature and thickness variations of the IPL are evident. **b**, SACs projected along a tangential axis, after piecewise bilinear alignment to the tangential plane. **c**, SAC stratification profiles before (dashed) and after (solid) piecewise bilinear alignment. **d,** SAC stratification depth versus distance from the soma. Lines indicate median, and shading the 25th and 75th percentiles. Distance bins are 20 μm wide, beginning with 0 to 20 μm.

proximal zone, weakly in the intermediate zone, and is roughly constant in the distal zone (Fig. 2.5d).

CHAPTER 3

Classification of Bipolar Cells

Since

3.1. Morphological classification of Bipolar Cells

Only if the stratification profiles of two cells overlap is there potential for contact between the cells, and hence potential for synaptic connections. In other words, stratification constrains retinal connectivity [Masland, 2004]. It follows that cell types defined using stratification are likely to end up having functional significance, assuming that the connectivity of a cell is closely related to its function [Seung and Sümbül, 2014].

Off Bipolar Cells. BC stratification profiles were computed by dividing surface voxels into 100 bins spanning 0 to 100% IPL depth. Classification into cell types was done by using methods similar to those described previously [Helmstaedter et al., 2013]. The BCs were split into shallow (BC1/2) and deep (BC1/2) clusters using the 75th percentile depth of the stratification profile. The BC1/2 cluster was further subdivided by stratification width, defined as the difference between 75th and 25th percentile depths. The wider cluster was identified as BC2 and the narrower cluster as BC1, based on a molecular classification showing that BC2 has more cells per square millimeter than BC1 [Wässle et al., 2009]. This correspondence between structural and molecular classifications is the opposite of a previous report [Helmstaedter et al., 2013]. The discrepancy may be due to methodological differences, such as computing stratification profiles based on surface voxels versus skeletons. The BC3/4 cluster was subdivided into BC4 and BC3 by the 10th percentile depth, because the molecularly defined BC4 stratifies closer to the INL [Wässle et al., 2009]. Finally, BC3 was subdivided into BC3a and BC3b based on axonal arbor volume, with BC3a having the larger axonal volume. Fig. 3.2 shows that each of the above subdivision steps was based on a feature with a roughly bimodal histogram.

The result still contained a small number of classification errors, as adjacent BCs of the same type overlapped enough to violate the mosaic property. Corrections were made by an automatic algorithm that greedily swapped cells from one cluster to another such that the total overlap between convex hulls of cells of a given type was minimized. Two swaps were vetoed by an expert (J.S.K) on the basis of morphological features. In all, six cells were swapped within BC1/2 and 13 within BC3/4. In the final classification, 41, 56, 29, 35, and 34 BCs were identified as types 1, 2, 3a, 3b, and 4, respectively. A few cells that violated the mosaic of all types and had irregular stratification profiles were discarded as possible reconstruction errors or amacrine cells.

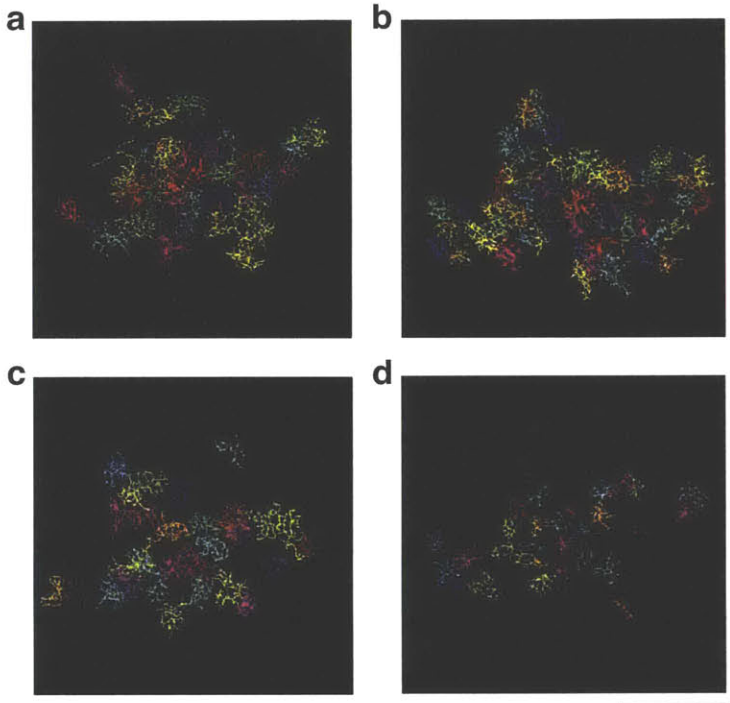

Type	n	Hull Area	Density	Overlap
BC1	41	382±104	3652	40%
BC2	56	297±79	4485	33%
BC3a	29	363±103	3236	18%
BC3b	35	206±57	5418	11%
BC4	34	266±114	4303	15%

FIGURE 3.1. Off BC types

Off BC types 1, 2, 3a, 3b, and 4 (**a** through **e**, respectively). BC1/2 mosaics appear complete. BC3/4 mosaics show some gaps, probably because some of the thin axons of BC3/4 were missed in the INL. **f**, Statistics of off BC types in this volume. Means and standard deviation of the hull area (area of the convex hull around the cell) are measured in μm^2. Type densities are estimated by dividing the number of cells (n) by the total area covered by the union of the hulls of that cell type, and are measured in cells/mm^2 without compensation for tissue shrinkage (Methods). Up to an overall scale factor, our densities are similar to those of Wässle et al. [2009], who found 2233, 3212, 1866, 3254, and 3005 cells/mm^2 for molecularly identified BC types, ordered as in the table.

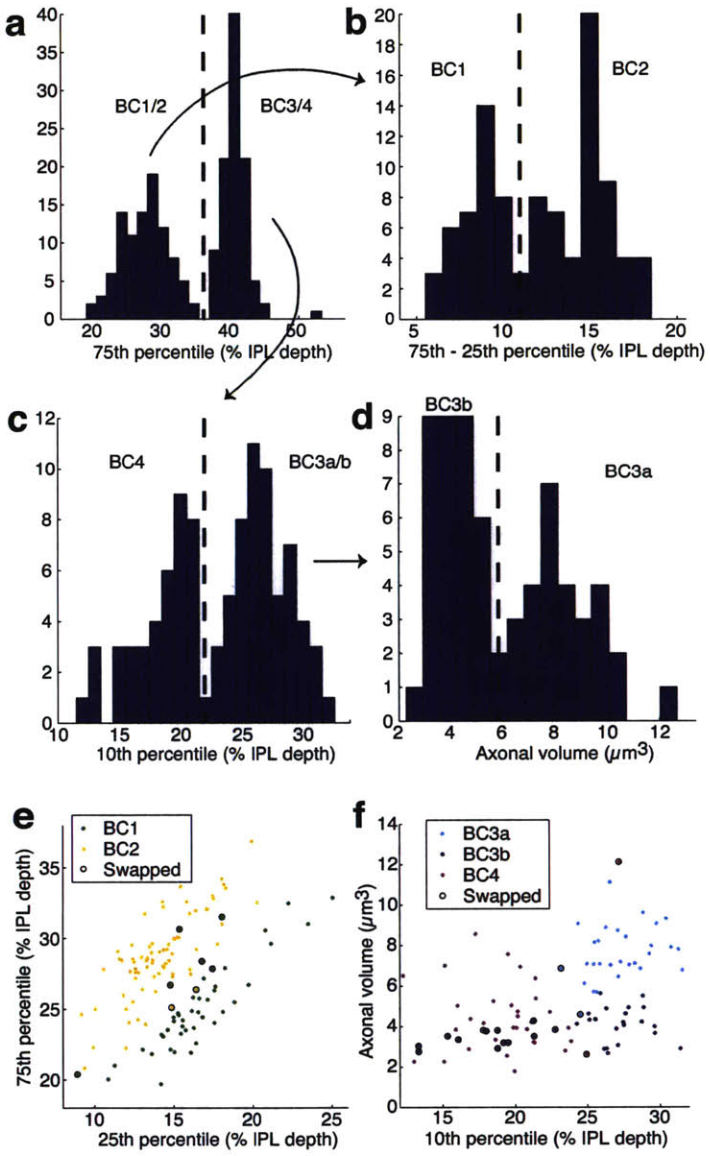

FIGURE 3.2. Off BC classification.

BCs were clustered based on their stratification profiles and axonal volumes. **a**, Cells were split into two clusters by the IPL depth of the 75th percentile of their stratification profiles. **b**, The shallow cluster BC1/2 was separated into BC1 and BC2 using stratification width, defined as the difference between 75th and 25th percentiles. **c**, The deep cluster BC3/4 was divided by 10th percentile into BC4 and BC3. **d**, BC3 was divided by axonal volume to yield BC3a and BC3b. Scatter plots of the (**e**) BC 1/2 and (**f**) BC 3/4 divisions show swaps that were made to eliminate mosaic violations. No swaps between BC 1/2 and BC 3/4 were needed.

On Bipolar Cells. We define the stratification profile as the density of surface area versus depth in the IPL. For the purpose of BC classification, we restricted the domain of the stratification profile to the interval between IPL depth 0.4 and 1. The domain omitted depths between 0 and 0.4 to exclude the trunks of the axonal arbors, which increase variability of the stratification profiles. Each stratification profile is normalized like a probability density, so that profile area between IPL depths 0.4 and 1 integrates to unity. Since IPL depth is dimensionless, the stratification profile is also dimensionless. Helmstaedter et al. [2013] defined stratification profile as the density of reconstructed skeleton. This definition is slightly different from ours, but yields similar results (data not shown). Percentiles are defined for a stratification profile, in the same way as for a probability density. Namely, the interval from the nth percentile depth to 0th percentile depth contains n percent of the area of the stratification profile. As mentioned earlier, 0th percentile depth is defined as IPL depth 0.4. The thickness of the stratification profile is defined as the difference between 85th and 25th percentile depths. Helmstaedter et al. [2013] defined thickness as the difference between 75th and 25th percentile depths, which yields similar classifications. In addition to stratification, we characterized single cell anatomy by a further property, the area of the cell's projection onto the tangential (xy) plane.

We hierarchically clustered our On BCs as follows. The axonal arbors of BC5 and XBC lie between the Off and On SACs. Accordingly, a BC5/XBC cluster separates from other types based on 85th percentile depth (Fig. 3.3a). This cluster in turn subdivides by 25th percentile depth into outer (closer to the INL) and inner (closer to the GCL) clusters (Fig. 3.3b). The outer cluster can be divided into BC5t and BC5o; the former is more thickly stratified than the latter (Fig. 3.3d). The inner cluster divides into XBC and BC5i based on projection area (Fig. 3.3e).

Types outside the BC5/XBC cluster lie between the On SACs and GCL. BC7 separates from the others by 85th percentile depth (Fig. 3.3a). Then BC6, BC8/9, and RBC separate from each other based on projection area (Fig. 3.3c). We chose not to separate BC8 and BC9, as the reconstructed cells were too few to yield two complete tilings.

BC8, BC9, and RBC all appear underrepresented relative to Helmstaedter et al. [2013]. This discrepancy could be artifactual, caused by failures to identify the relatively thin axons of these three types in the interstices of the INL. Alternatively, these cell types might be truly underrepresented in our volume.

Histograms showing the various splits in the hierarchical clustering are shown in Fig. 3.3. The splits are highly convincing near the top of the hierarchy, but less convincing near the bottom. Therefore we sought further validation from the principle that the arbors of a bipolar cell type should "tile" the retina with little overlap. If the hierarchical clustering yields cell types that tile the retina, that would be independent validation of the clustering, which relied only on anatomical properties of single cells. For all types, few violations of the tiling principle were observed (Fig. 3.4e, f, g). There are some holes in the tilings, but they are likely the result of omissions in cell reconstruction rather than classification errors. Violations of tiling can be rectified by swapping cells between types, to yield improved classifications. The fraction of swapped cells is small.

mouse BCs were originally classified into nine cone types (BC1 through BC9) and one rod type based on light microscopic anatomy [Ghosh et al., 2004]. Later on,

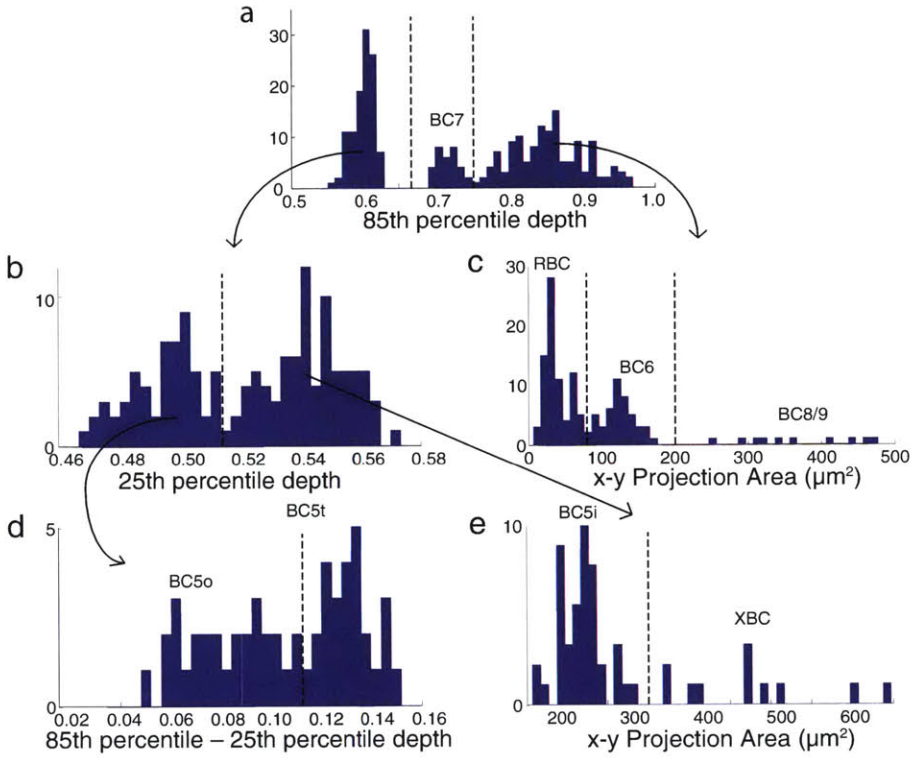

FIGURE 3.3. On BC classification.
Hierarchical clustering procedure for On BCs based primarily on percentiles of the stratification profile. Dashed lines show locations of dividing points. **a**, BCs are initially subdivided into three groups by 85th percentile IPL depth. **b**, BC5 types and XBC are further divided by 25th percentile IPL depth. **c**, RBC, BC6 and BC8/9 are distinguished by the total area of their projection onto the xy plane. Due to the sparse representation of BC8/9 in our set of reconstructed cells, we were unable to subdivide it. **d**, BC5t and BC5o are differentiated by stratification thickness, as defined by the difference between a cell's 85th and 25th percentile IPL depths. **e**, BC5i and XBC differ in the total area of their projection onto the xy plane.

BC3 was subdivided into BC3a and BC3b based on molecular differences [Wässle et al., 2009]. Then electron microscopic anatomy was used to distinguish BC3a and BC3b, divide BC5 into two types, and discover a new XBC type [Helmstaedter et al., 2013].

We revisited the classification of On BCs using the e2198 reconstructions (Fig. 3.3). As shown in the gallery of example cells (Fig. 3.4a, b), On BC axons are found in half the depth of the IPL, closer to the GCL than the INL. Our On BC types correspond to those defined previously, with good agreement regarding densities (compare Fig. 3D with Fig. 1E inset of [Helmstaedter et al., 2013]).

The novelty is the subdivision of BC5 into three types called BC5t, BC5i, and BC5o. The three types stratify at similar depths (Fig. 3.4a, c), which is why they were originally grouped into a single Type 5 [Ghosh et al., 2004]. Nevertheless, it is possible to differentiate between the types based on subtle differences between their stratification profiles. BC5-inner ("BC5i") stratifies slightly more towards the inner retina than the other types (Fig. 3.4a, b and Fig. 3.3b). BC5-thick ("BC5t") is more thickly stratified than BC5-outer ("BC5o"), as shown in Fig. 3.4a, c and Fig. 3.3d. The stratification profile of BC5t is weakly bimodal (Fig. 3.4c), but this property was not used for the classification.

We are confident of our three-way division of BC5 based on stratification (Fig. 3.31), because the axonal arbors of each cluster end up roughly tiling the retina with little overlap (Fig. 3.4e, f, g). This "tiling principle" is thought to be a defining characteristic of a true bipolar cell type [Wässle et al., 2009]. On the other hand, when BC5 cells are divided into just two clusters, it is impossible to avoid many collisions between highly overlapping axonal arbors (Fig. 3.5e).

Only a few violations of the tiling principle are evident in Fig. 3.4e, f, and g. One possibility is that the tiling principle holds only approximately, and that the violations are a form of biological "noise." Another possibility is that the violations result from errors in our classification procedure. Therefore, we generated a "corrected" classification by swapping a few cells between types. The number of swaps is relatively small. The corrected classification was the basis of subsequent analysis of BC-SAC wiring, but our results are qualitatively unchanged even if the uncorrected classification is used.

3.2. Classification by Connectivity

It would be more direct to define a cell type as a set of cells with similar contact or connectivity patterns [Seung, 2009, 2012], rather than use stratification as a proxy for these properties. For example, the 302 neurons of *C. elegans* were divided into 118 classes, each containing neurons with similar connectivity patterns [White et al., 1986]. Likewise Helmstaedter et al. [2013] divided BC5 into classes based on patterns of contact with two ganglion cell types named "gc31-56" and "gc36-51." We decided to replicate their analysis, mainly in order to determine the correspondence between contact-based and stratification-based classifications. A secondary motivation was to examine how contact-based classification depends on the completeness of reconstruction. Helmstaedter et al. [2013] reconstructed all neurons with cell bodies contained in a $(0.1\ \text{mm})^2$ patch. This method missed ganglion cells with arbors inside the patch but cell bodies outside the patch, which is why gaps in coverage are visible in the gallery of cell types provided in the Supplementary Data of Helmstaedter et al. [2013]. Contact with missing arbors obviously cannot be quantified, hampering contact-based classification.

We were able to replicate and improve the contact-based classification by making use of a large set of ganglion cells that were reconstructed from the e2198 dataset in a parallel study to be reported elsewhere. From this set of ganglion cells, we identified 16 examples of gc31-56 and 19 examples of gc36-51 based on their distinctive stratification profiles (Fig. 3.5a, b). The arbors of each ganglion cell type completely cover the central region of e2198 where the bipolar cells are located, because the reconstructed ganglion cells include those with cell bodies outside the central region. For each BC5 cell, we quantified the fraction of its axonal surface

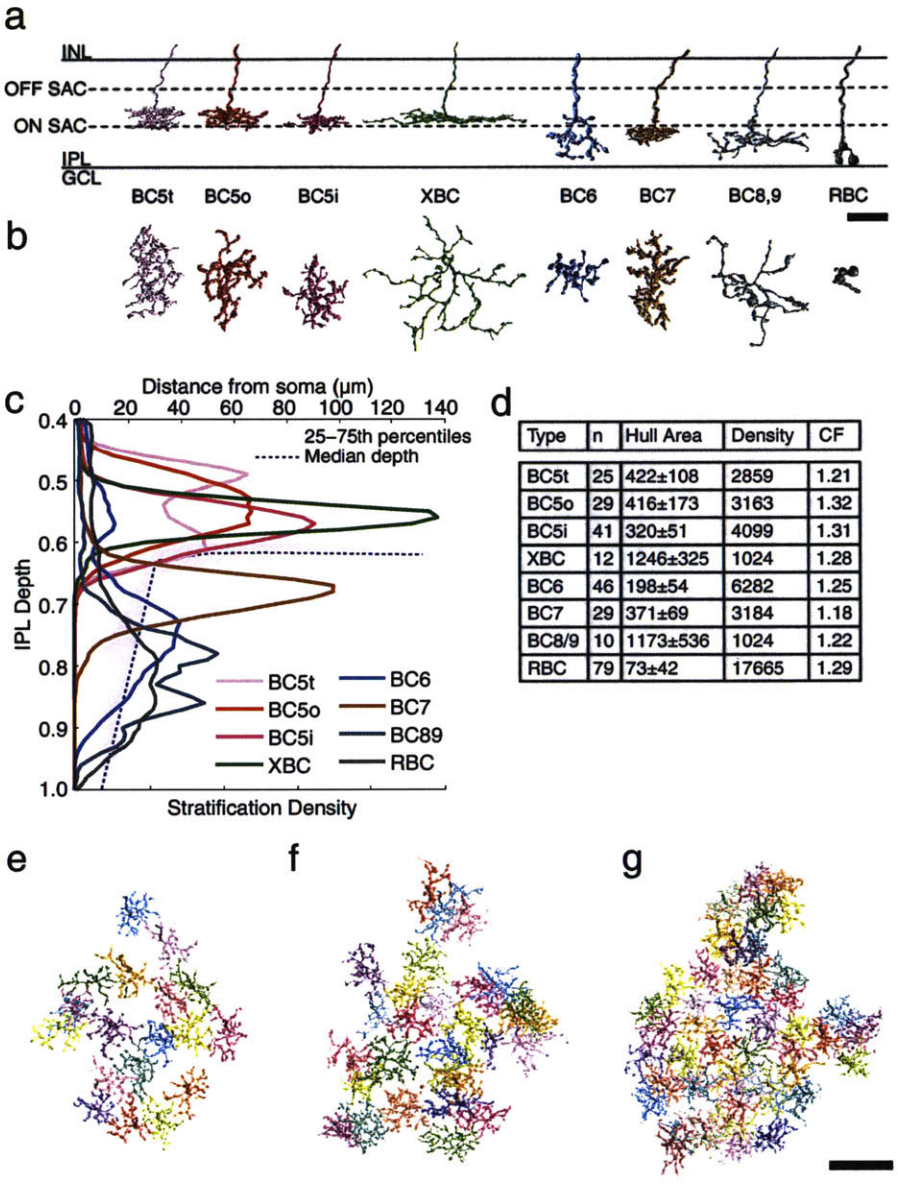

Type	n	Hull Area	Density	CF
BC5t	25	422±108	2859	1.21
BC5o	29	416±173	3163	1.32
BC5i	41	320±51	4099	1.31
XBC	12	1246±325	1024	1.28
BC6	46	198±54	6282	1.25
BC7	29	371±69	3184	1.18
BC8/9	10	1173±536	1024	1.22
RBC	79	73±42	17665	1.29

FIGURE 3.4. Classification of On BC types.
Examples of each type, perpendicular (**a**) and parallel (**b**) to light axis. (**c**) Average stratification profiles of types, along with median (dashed line) and quartiles (shaded) of stratification depth of On SAC dendrites versus distance from SAC cell body. (**d**) Table of statistics: number n of reconstructed cells; average convex hull area of the projection onto the plane perpendicular to the light axis; estimate of number of cells per mm^2; coverage factor, sum of convex hull areas divided by area of hull union. BC5t (**e**), BC5o (**f**), and BC5i (**g**) axonal arbors show few violations of the tiling principle, suggesting that the classification is fairly accurate. Scale bars, 10 μm for **a**, **b** and 30 μm for **e**, **f**, **g**.

area in contact with gc31-56 cells, and the fraction of its axonal area in contact with gc36-51 cells. Then BC5 indeed splits nicely into two clusters based on the two contact fractions (Fig. 3.5c). One cluster, named "BC5A" by Helmstaedter et al. [2013], has more contact with gc31-56. BC5A tiles with few violations (Fig. 3.5e) and therefore appears to be a pure cell type. BC5A corresponds almost exactly with BC5i (Fig. 3.5c).

The other cluster, named "BC5R" by Helmstaedter et al. [2013], has more contact with gc36-51. Because BC5R contains many tiling violations (Fig. 3.5e), Helmstaedter et al. [2013] speculated that BC5R was a mixture of more than one type. Our stratification-based classification confirms their speculation by effectively dividing BC5R into BC5o and BC5t, both of which tile the retina separately.

The cleanness of the division between BC5A and BC5R is evident in a histogram of the difference between the gc31-56 and gc36-51 contact fractions, in which two well-separated clusters are evident (Fig. 3.5d). Note that Helmstaedter et al. [2013] labeled some of their reconstructed cells as BC5X. This name was not intended to be a type but rather indicated cells that were unclassifiable because they lacked contact with gc31-56 and gc36-51. We do not have this problem because our coverage of the ganglion cell types is more complete.

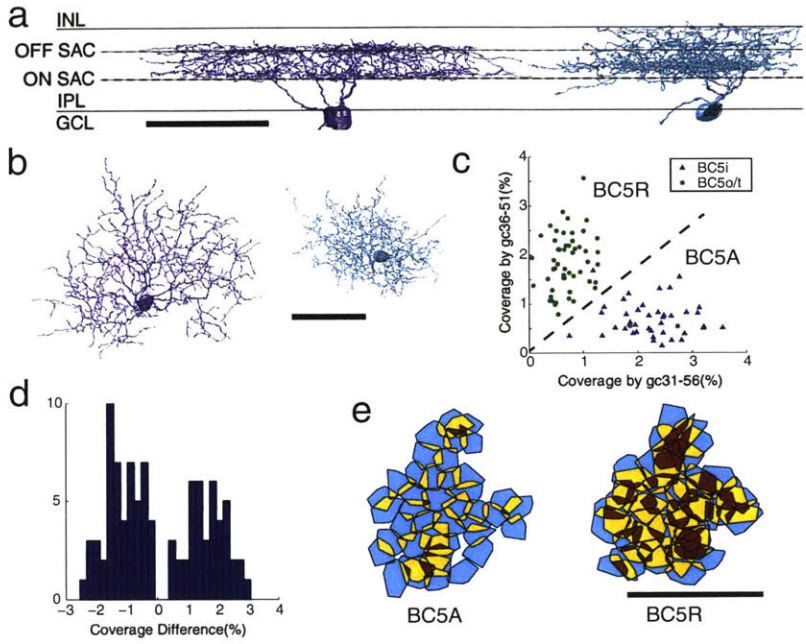

FIGURE 3.5. Contact-based division of BC5.
Two-way division of BC5 into BC5A and BC5R, defined by contact with ganglion cell types using the method of Helmstaedter et al. [2013]. **a, b**, Representative examples of gc31-56 (blue) and gc36-51 (green), shown perpendicular and parallel to light axis. **c**, Each data point represents one BC5 cell, and the coordinates for each cell are the fraction of the BC5 axon in contact with gc36-51 and gc31-56. The dashed diagonal line separates the points into two clusters, named BC5A and BC5R. The color/shape of each symbol indicates whether the cell was classified as BC5i versus BC5t or BC5o based on single cell anatomy and the procedure of Fig. 3.3. BC5A corresponds almost perfectly with BC5i, and BC5R with BC5t/o. **d**, Histogram of the same data points as in the previous xy plot, but binned by the difference between the x and y coordinates, i.e., coverage by gc31-56 minus coverage by gc36-51. The histogram separates nicely into BC5R and BC5A clusters. **e**, Convex hulls of BC5 cells with two-cell overlap in yellow and three or greater cell overlap in red. BC5A tiles well, while BC5R contains many tiling violations. Scale bar, 100 μm.

CHAPTER 4

Direction Selectivity in the Off SAC

The starburst amacrine cell is a critical player in the direction selectivity circuit. A SAC dendrite is more activated by motion outward from the cell body to the tip of the dendrite, than by motion in the opposite direction [Euler et al., 2002]. Therefore a SAC dendrite exhibits DS, and outward motion is said to be its "preferred direction." Note that it is incorrect to assign a single such direction to a SAC, because each of the cell's dendrites has its own preferred direction (Fig. 3.1a). DS persists after blocking inhibitory synaptic transmission [Hausselt et al., 2007], when the only remaining inputs to SACs are bipolar cells (BCs), which are excitatory. Since the SAC exhibits DS, while its BC inputs do not [Yonehara et al., 2013], we say that DS *emerges* from the BC-SAC circuit.

Mouse BCs have been classified into multiple types [Wässle et al., 2009], with different time lags in visual response [Baden et al., 2013, Borghuis et al., 2013]. Motion is a spatiotemporal phenomenon: an object at one location appears somewhere else after a time delay. Therefore we wondered whether DS might arise because different locations on the SAC dendrite are wired to BC types with different time lags. More specifically, we hypothesized that the proximal BCs (wired near the SAC soma) lag the distal BCs (wired far from the soma).

Such "space-time wiring specificity" could lead to DS as follows (Fig. 1.2c). Motion outward from the soma will activate the proximal BCs followed by the distal BCs. If the stimulus speed is appropriate for the time lag, signals from both BC groups will reach the SAC dendrite simultaneously, summing to produce a large depolarization. For motion inward towards the soma, BC signals will reach the SAC dendrite asynchronously, causing only small depolarizations. Therefore the dendrite will "prefer" outward motion, as observed experimentally [Euler et al., 2002].

4.1. Contact analysis

We reconstructed 195 Off BC axons and 79 Off SACs from e2198 (Fig. 2.4b). The e2198 retina was stained in an unconventional way that did not mark intracellular structures such as neurotransmitter vesicles [Briggman et al., 2011], and reliable morphological criteria for identification of BC presynaptic terminals are unknown. As an indirect measure of connectivity, contact areas were computed for all BC-SAC pairs. The resulting "contact matrix" was analyzed through two subsequent steps.

In the first step, Off BC axons were classified into five cell types, following structural criteria [Helmstaedter et al., 2013] established to correspond with previous molecular definitions [Wässle et al., 2009] (Fig. 3.2). BC types stratify at characteristic depths in the inner plexiform layer (IPL), and vary in size (Fig. 4.1a). The BCs of each type formed a "mosaic," meaning that cells were spaced roughly

periodically (Fig. 3.1a-e). This is generally accepted as an important defining property of a retinal cell type. Type densities (Fig. 3.1f) were roughly consistent with previous reports [Wässle et al., 2009]. When the columns of the contact matrix were sorted by BC type (Fig. 4.1b), it became evident that BC2 and BC3a contact SACs more than other BC types.

In the second step, we averaged contact area over BC-SAC pairs of the same BC type and similar distance between the BC axon and the SAC soma in the plane tangential to the retina (Fig. 4.1c). These absolute areas were normalized to convert them into the percentage of SAC surface area covered by BCs of a given type (Methods). The resulting graphs show that BC2 prefers to contact SAC dendrites close to the SAC soma, whereas BC3a prefers to contact far from the soma (Fig. 4.1d, Fig. 4.2c).

Edges of the affinity graph connecting BC with SAC voxels were defined as BC-SAC contact edges. For each pair, the sum of the edges yielded an estimate of contact area. The Euclidean distance separating each BC-SAC pair was computed after projecting their centers onto the SAC plane. Centers of SAC somata were manually annotated, and centers of BC arbors were computed as the centroids of their surface voxels. The pairs were binned by distance of the BC from the SAC soma. For every pair in a bin, the fraction of SAC surface area devoted to BC-SAC contact within the convex hull of the BC was computed as the ratio of BC-SAC contact edges to SAC surface edges within the convex hull. The latter was estimated by the number of SAC surface voxels multiplied by a geometric conversion factor of 1.4 SAC surface edges per surface voxel. (This factor was estimated by dividing the total number of SAC surface edges by the total number of SAC surface voxels in the volume.) BC-SAC pairs with fewer than 10,000 SAC surface voxels inside the hull were excluded from the computation to reduce the effect of fluctuations. The ratios for BCs of the same type were averaged for each distance bin and multiplied by a mosaic overlap factor to yield the values in Fig. 4.1d. The mosaic overlap factor represents the extent to which neighboring convex hulls overlap one another, which varies by cell type. This factor was computed by dividing the sum of the hull areas for each cell by the area of the union of hulls for each cell type.

In instances where edges in the affinity graph are converted to area in μm^2, the conversion factor of $291.5\mu m^2$ per edge is used. This factor estimates the real surface area of the cell given the different possible orientations of edges and effects from pixelization.

4.2. Co-stratification analysis

Off SACs stratify at a particular depth in the IPL (Fig. 4.3a). Why this depth and not some other? From Fig. 4.1a, it is obvious that this depth is appropriate for wiring with BC2 and BC3a, as required by our model of DS emergence. Following this logic one step further, we wondered whether the observed dependence of contact on distance from the SAC soma might be reflected in fine aspects of SAC morphology. We hypothesized that SAC dendrites are "tilted," moving deeper into the IPL with distance from the SAC soma. Such a change in depth would be compatible with more overlap with BC2 near the soma, and more overlap with BC3a far from the soma, since BC3a is deeper in the IPL than BC2 (Fig. 4.1a).

The hypothesized tilt turns out to exist (Fig. 4.3a). Very close to the SAC soma, the dendrites dive sharply into the IPL from the INL. Surprisingly, IPL depth

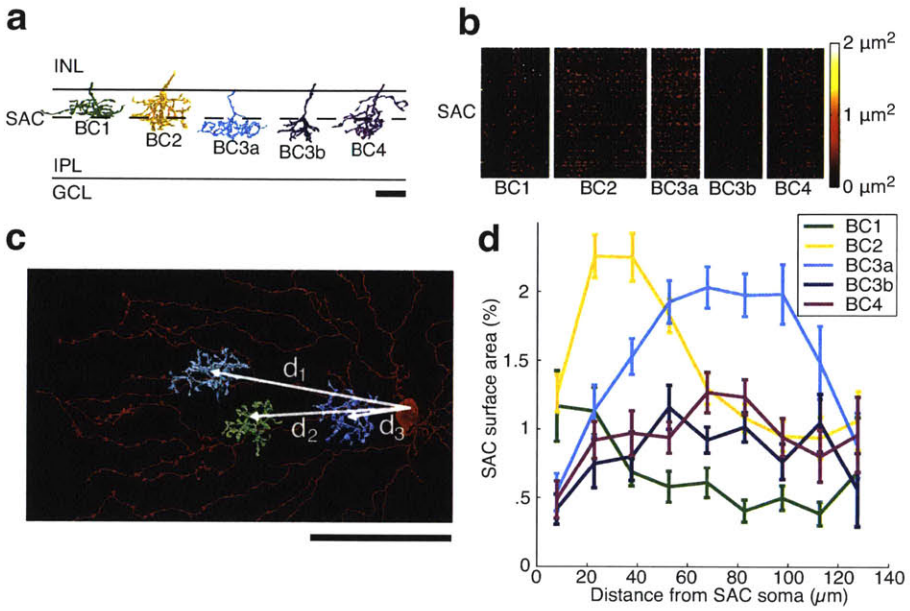

FIGURE 4.1. BC-Off SAC contact.
a, Off BCs were divided into five types Wässle et al. [2009], Helmstaedter et al. [2013], based on IPL depth and size. Scale bar is 10 μm. **b**, Contact areas of BC-SAC pairs, sorted by BC types. **c**, Pairs were further sorted by the distance of the BC axon from the SAC soma, as measured in the tangential plane. Scale bar is 50 μm. **d**, Average BC-SAC contact vs. distance, normalized to percentage of SAC surface area at that distance. Standard error is based on the number of pairs for each BC type and distance.

continues to increase as distance from the SAC soma in the tangential plane ranges from 20 to 80 μm. The slight increase is not evident in a single dendrite, but emerges from statistical averaging.

Could dendritic tilt be the cause of the observed variation in BC-SAC contact with distance (Fig. 4.1d)? We cannot address causality based on our data, but we can test how well the tilt predicts contact variation. We computed the stratification profiles of BC types (Fig. 4.3a), defined as the one-dimensional density of BC surface area along the depth of the IPL. We also computed the stratification profile of SAC dendrites at various distances from the SAC soma (quartiles, Fig. 4.3a). Assuming that BC and SAC arbors are statistically independent of each other, we estimated contact from "co-stratification," defined as the integral over IPL depth of the product of BC and SAC stratification profiles (Methods).

We found that actual BC2 contact depends more strongly on distance than predicted; the slight change in IPL depth after the initial plunge appears too small to account for the large change in actual BC2 contact. In other failures of contact prediction, BC3a, BC3b, and BC4 stratify at the same IPL depths (Fig. 4.3a), yet BC3a makes much more contact than BC3b or BC4. Also, actual BC3a contact

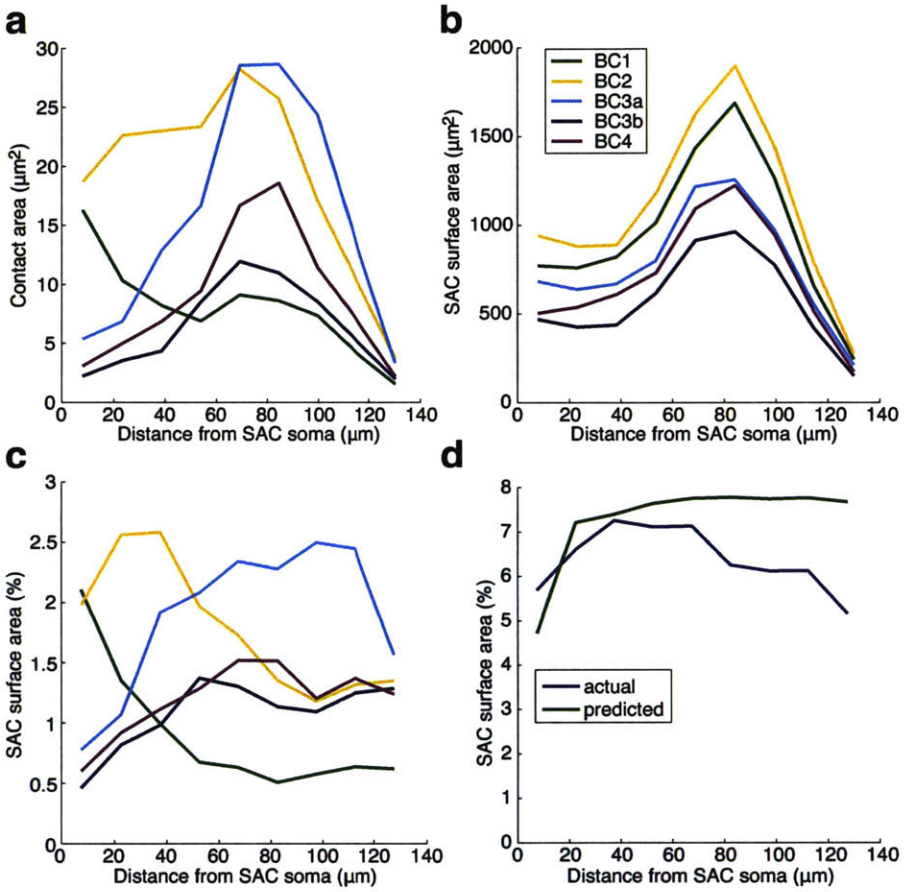

FIGURE 4.2. Alternative contact analysis.
Alternative contact analysis based on total areas rather than averages over individual pairs. **a,** Total contact observed between all reconstructed BCs and SACs as a function of distance from the SAC soma. **b,** Total SAC surface area within the union of convex hulls of each BC type as a function of distance from the SAC soma. All graphs are peaked around 80 μm, which is the region of maximum SAC dendritic branching. The sharp decrease at larger distances is due to thinning and termination of SAC branches. The graphs differ across BC types, because the types do not cover exactly the same retinal areas. **c,** Fraction of SAC surface area in contact with BC types, estimated by dividing contact area (**a**) by SAC surface area (**b**). This estimate is similar to that of Fig. 4.1d, but lacks error bars. **d,** Fraction of SAC surface area contacted by all BC types, obtained as the sum of the contact fractions in (**c**). Also plotted for comparison is the contact predicted by co-stratification, the sum of the curves from Fig. 4.3b.

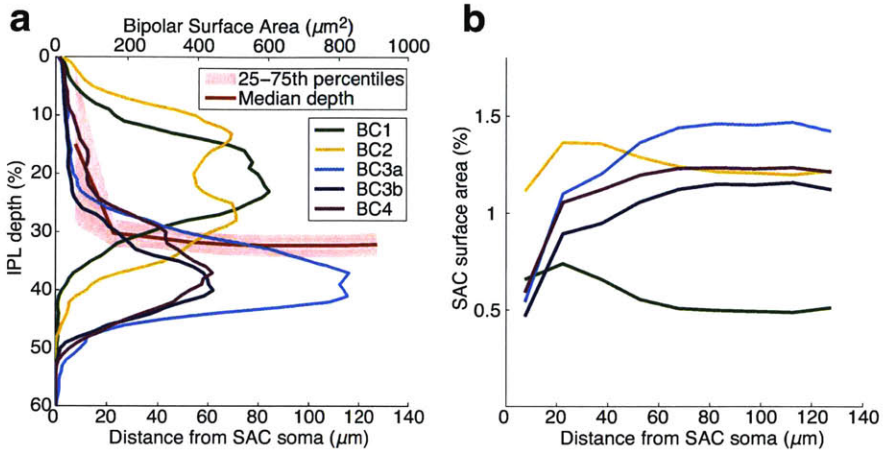

FIGURE 4.3. BC-SAC co-stratification.
a, SAC dendrites move deeper into the IPL (median depth, red line) with increasing distance from the SAC soma in the tangential plane. Stratification profiles of BC types, defined as density of surface area over the depth of the IPL. **b**, Co-stratification predictions of BC-SAC contact area vs. distance from the SAC soma. The curves are normalized by SAC area at each distance, and are therefore directly comparable with those of Fig. 4.1d.

plummets near the tips of SAC dendrites (Fig. 4.1d), while predicted contact does not change at all because the IPL depth of SAC dendrites is constant in this region (Fig. 4.3b). Overall, the total contact from all BC types seems low in this region (Fig. 4.2d), suggesting that BCs avoid making synaptic inputs to the most distal SAC dendrites. This runs counter to the conventional belief that input synapses are uniformly distributed over the entire length of SAC dendrites [Famiglietti, 1991]. The unreliability of inferring contact from co-stratification is illustrated by numerous examples of SAC dendrites that pass through BC axonal arbors without making any contact at all (Fig. 2.1).

To perform these analyses, all SAC surface voxels were binned by distance from the soma center in the SAC plane. Within each bin, the stratification profile was computed as for the BCs. The quartiles (median and 25th and 75th percentiles) are graphed in Fig. 4.3a. The prediction of contact from co-stratification is based on the following formalism.

We define the arbor density $\rho_a(\vec{r})$ as the surface area per unit volume at location $\vec{r}$ of a type a cell with soma centered at the origin. Its integral $\int d^3r\, \rho_a(\vec{r})$ is the total surface area of the arbor. We assume that the contact density received by one cell of type a from all cells of type b is equal to

$$c_{ab}(\vec{r}) = \rho_a(\vec{r}) \sum_i \rho_b(\vec{r} - \vec{r}_{bi}) \tag{4.2.1}$$

The sum over the b mosaic can be approximated by a function that is independent of x and y,

$$\sum_i \rho_b(\vec{r} - \vec{r}_{bi}) \approx \sigma_b s_b(z) \tag{4.2.2}$$

where σ_b is the number of type b neurons per retinal area and

$$s_b(z) = \int dxdy\, \rho_b(x, y, z) \tag{4.2.3}$$

is the stratification profile of a cell of type b. The SAC arbor density is assumed radially symmetric, $\rho_{SAC}(\vec{r}) = \rho_{SAC}\left(\sqrt{x^2+y^2}, z\right)$, where ϕ can be regarded (up to normalization) as the SAC stratification profile as a function of distance $r = \sqrt{x^2+y^2}$ from the SAC soma. Integrating the contact density (Fig. 4.2.1) and normalizing yields the fraction $\phi_b(r)$ of SAC area contacted by cell type b as a function of r,

$$\phi_b(r) = \sigma_b \frac{\int dz\, \rho_{SAC}(r, z) s_b(z)}{\int dz\, \rho_{SAC}(r, z)} \tag{4.2.4}$$

4.3. Model of direction selectivity

Imaging of intracellular calcium in BC axons [Baden et al., 2013] and extracellular glutamate around BC axons [Borghuis et al., 2013] indicate that the onset in visual response of BC2 occurs 50 to 100 ms later than that of BC3a. Therefore BC-SAC wiring appears to possess the space-time specificity appropriate for an outward preferred direction, as we hypothesize (Fig. 4.4c).

There is another important difference between BC2 and BC3a: BC3a responds more transiently to step changes in illumination, while BC2 exhibits more sustained responses. The implications of the sustained-transient distinction for DS can be understood using a mathematical model. The activity of a retinal neuron is often approximated as a linear spatiotemporal filtering of the visual stimulus followed by a nonlinearity [Berry and Meister, 1998, Baccus and Meister, 2002]. Such a "linear-nonlinear" model for the output $O(t)$ of the SAC dendrite can be written as

$$O(t) = \left[\int dxdt'\, W(x, t-t') I(x, t')\right]^+ \tag{4.3.1}$$

For simplicity, the dendrite and visual stimulus $I(x, t)$ are restricted to a single spatial dimension x, and the nonlinearity is a half-wave rectification, $[z]^+ = \max\{z, 0\}$. We interpret the integral in Eq. (Fig. 4.3.1) as the summed input from the BCs presynaptic to the SAC. The nonlinearity could arise from various biophysical mechanisms, such as synaptic transmission from SACs to other neurons. The spatiotemporal filter $W(x, t)$ is a sum of two functions,

$$W(x, t) = U_s(x) v_s(t) + U_t(x) v_t(t) \tag{4.3.2}$$

corresponding to contributions from BC2 and BC3a. The sustained temporal filter $v_s(t)$ is monophasic, while the transient filter $v_t(t)$ is biphasic (Fig. 4.4a). The spatial filter $U_s(x)$ represents the entire set of all BC2 inputs to the dendrite, and can be estimated from the BC2 contact area graph in Fig. 4.1d. Similarly, $U_t(x)$ can be estimated from the BC3a contact area graph. The two spatial filters are displaced relative to each other (Fig. 4.4a), because BC3a tends to contact SAC dendrites at more distal locations than BC2.

It is well known that direction selectivity (DS) can be generated by a model like Eqs. (Fig. 4.3.1) and (Fig. 4.3.2), which is based on the sum of two space-time separable filters [Watson and Ahumada, 1985, Adelson and Bergen, 1985]. This is illustrated by Fig. 4.5 6 using the fact that the convolution in Eq. (Fig. 4.3.1) is equivalent to "sliding" the spatiotemporal filter W in time over the stimulus I, and computing the overlap at each time. The filter $W(x,t)$ is oriented in space-time (Fig. 4.4a), and so also is a moving stimulus $I(x,t)$ (Fig. 4.4g,h). The overlap with a rightward-moving stimulus (Fig. 4.4h) is greater than for a leftward one (Fig. 4.4g), so the model is DS, and rightward is the preferred direction.

How is DS affected by the biphasic shape of the transient temporal filter, $v_t(t)$? If we remove the negative lobe (Fig. 4.4c), then $v_t(t)$ will become monophasic like $v_s(t)$ and their relation closer to a simple time lag (Fig. 4.4d). We will refer to this model as a "Reichardt detector," in honor of the pioneering researcher Werner Reichardt, although it more closely resembles a subunit of his model Reichardt [1961]. On the other hand, removing the positive lobe of $v_t(t)$ makes it monophasic but with inverted sign relative to the sustained filter (Fig. 4.4e). The result (Fig. 4.4f) resembles a DS model originally proposed by Barlow and Levick [Barlow and Levick, 1965].

Both modified models (Fig. 4.4d,f) exhibit DS. In the Reichardt detector, the inputs from the two arms enhance each other for motion in the preferred direction. In the Barlow-Levick detector, the two inputs cancel each other for motion in the null direction. Since our sustained-transient model (Fig. 4.4b) employs both mechanisms, it should exhibit more DS than either detector. Our model is related to versions of the Reichardt detector with low-pass and high-pass filters on the two arms [Borst et al., 2003].

In the original Barlow-Levick model, the negative filter corresponded to synaptic inhibition. Since BCs are believed to be excitatory, negative BC input in our model represents a reduction of excitation relative to the resting level, rather than true inhibition. Signaling by reduced excitation may be possible, at least for low contrast stimuli, as BC ribbon synapses may have a significant resting rate of transmitter release [Lagnado et al., 1996].

The model of Eqs. (4.3.1) and (4.3.2) is a useful starting point for many theoretical investigations that are outside the scope of this article. For example, DS dependences on the spatial and temporal frequency of a sinusoidal traveling wave stimulus are calculated in the Supplementary Equations, and DS dependence on stimulus speed is graphed in Fig. 4.5.

Mathematical model of the BC-SAC circuit. The output $O(t)$ of a SAC dendrite is modeled as

$$O(t) = g\left(\sum_{i=1}^{n} c_i f_i\left(\int dx dt' w_i(x, t-t') I(x,t')\right)\right) \tag{4.3.3}$$

The dendrite and the visual stimulus $I(x,t)$ are restricted for simplicity to a single spatial dimension x. The ith BC filters the visual stimulus with $w_i(x,t)$, and the result is passed through the nonlinear function f_i. The contributions from the BCs are weighted by the $c_i < 0$, summed, and passed through a nonlinear function g.

Suppose that $f_i(z) = [z + b_i]^+$ with $b_i > 0$ corresponding to spontaneous output in the absence of visual stimulation. Then the BC output nonlinearity can be neglected for visual stimuli with sufficiently small amplitude. Also suppose that

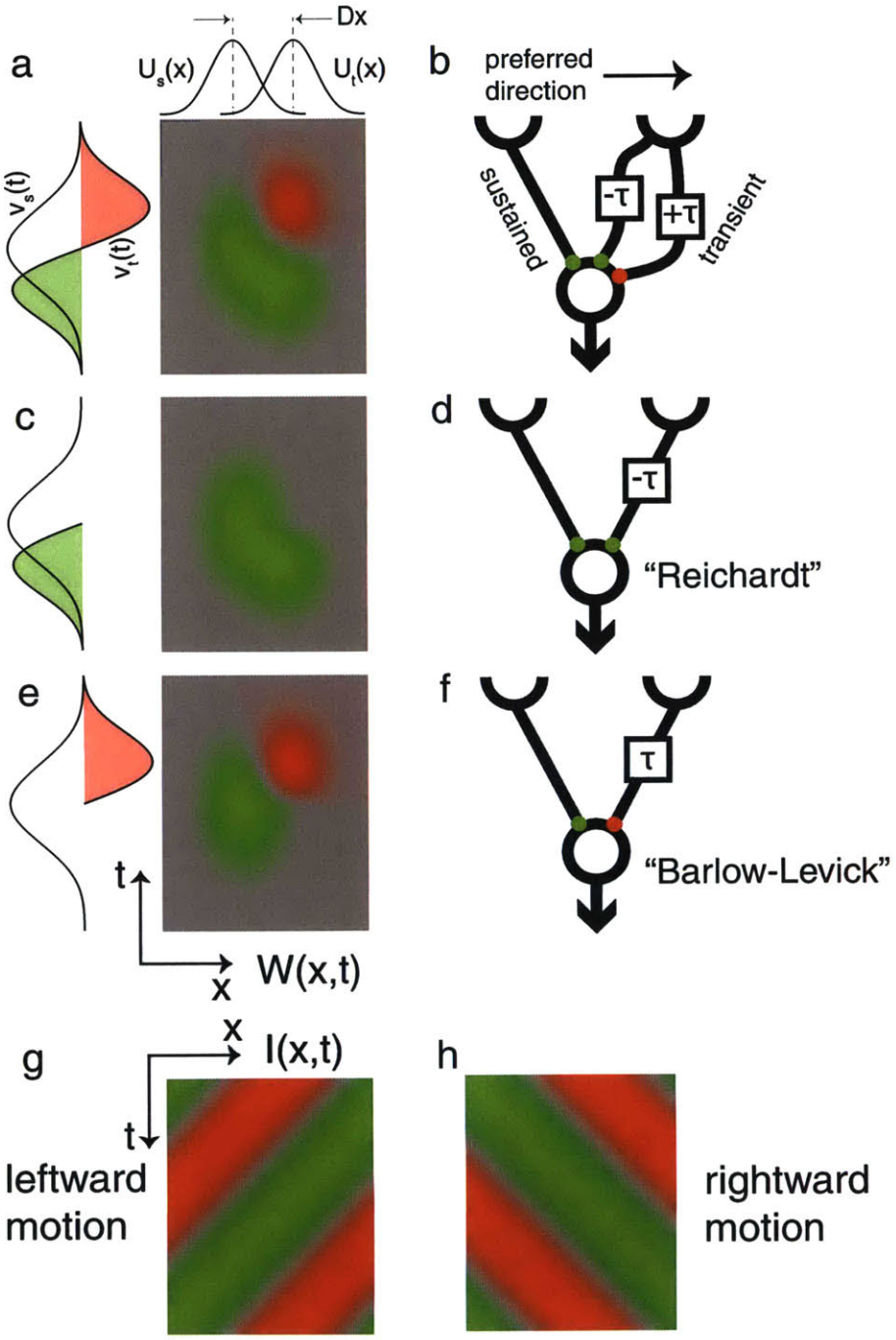

FIGURE 4.4. Mathematical model of the BC-SAC circuit.
a, Spatiotemporal filter of Eq. (4.3.2). Green is positive, red is negative, and gray is zero. **b**, The transient pathway effectively combines a positive channel that leads the sustained pathway by τ and a negative channel that lags by τ. **c**, Removing the negative channel yields a Reichardt detector (**d**). **e**, Removing the positive channel yields a Barlow-Levick detector (**f**). A moving visual stimulus $I(x,t)$ is oriented in space-time (**g**, **h**), and so are the spatiotemporal filters (**a**, **c**, **e**).

$g(z) = [z - a]^+$, where $a > 0$ corresponds to a threshold for SAC response, or some source of spontaneous inhibitory input. Then Eq. (4.3.3) simplifies to

$$O(t) = \left[\int dx dt' \sum_{i=1}^{n} c_i w_i(x, t - t') I(x, t') + \sum_i b_i c_i - a \right]^+ \tag{4.3.4}$$

Now assume that each spatiotemporal filter is separable, $w_i(x,t) \approx u_i(x)v_i(t)$, and that each temporal filter is either sustained or transient, $v_s(t)$ or $v_t(t)$. Then

$$\sum_i c_i w_i(x,t) \approx U_s(x)v_s(t) + U_t(x)v_t(t) \tag{4.3.5}$$

where $U_s(x) = \sum_{i \in S} c_i u_i(x)$ and $U_t(x) = \sum_{i \in T} c_i u_i(x)$ are the weighted sums of spatial filters over the sustained and transient sets of BCs. Finally, Eq. (4.3.4) reduces to Eq. (4.3.5) if $a = \sum_i b_i c_i$.

If the visual stimulus is a sinusoidal traveling wave, $I(x,t) = \cos(kx - \omega t)$, then the integral in Eq. (4.3.5) yields a sine wave given by the real part of

$$[\tilde{u}_s(k)\tilde{v}_s(\omega) + \tilde{u}_t(k)\tilde{v}_t(\omega)]\, e^{-i\omega t} = \tilde{u}_s(k)\tilde{v}_s(\omega) \left[1 - i\omega\tau e^{ik\Delta x}\right] e^{-i\omega t}$$

where $\tilde{u}_s(k) = \int dx\, e^{ikx} u_s(x)$ and other Fourier transforms are defined similarly. The amplitude of the sine wave defines the peak and time-averaged response of Eq. (4.3.5):

$$\begin{aligned} A(k,\omega) &= |\tilde{u}_s(k)|\, |\tilde{v}_s(\omega)|\, \left|1 - i\omega\tau e^{ik\Delta x}\right| \\ &= |\tilde{u}_s(k)|\, |\tilde{v}_s(\omega)|\, \sqrt{1 + 2\omega\tau \sin k\Delta x + (\omega\tau)^2} \end{aligned}$$

The term linear in ω is the DS component of the response. Assuming $\omega > 0$ and $\Delta x > 0$ without loss of generality, the preferred direction (PD) is rightward for spatial frequencies satisfying $|k\Delta x| < \pi$. Outside this range, spatial aliasing can cause the PD to reverse. The direction selectivity index (DSI) is

$$DSI = \frac{PD - ND}{PD} = 1 - \sqrt{\frac{1 - 2\omega\tau\, |\sin k\Delta x| + (\omega\tau)^2}{1 + 2\omega\tau\, |\sin k\Delta x| + (\omega\tau)^2}}$$

$$DSI = \frac{PD - ND}{PD} = 1 - \sqrt{\frac{1 - 2\omega\tau\, |\sin k\Delta x| + (\omega\tau)^2}{1 + 2\omega\tau\, |\sin k\Delta x| + (\omega\tau)^2}} \tag{4.3.6}$$

which can be rewritten as Eq. (4.3.6) in the main text. This is a periodic function of k, because the DSI is a ratio of responses. The responses themselves will typically vanish for large k, due to the spatial filtering, but the DSI is independent of the filter functions. According to the second line, $0 \leq DSI \leq 1$. The third line is maximized for any fixed ω when $k\Delta x = \pi/2$. This means that an optimal wavelength for the stimulus is $\lambda = 4\Delta x$. Then

$$DSI = 1 - \frac{1 - \omega\tau}{1 + \omega\tau}$$

which in turn is maximized when $\omega\tau = 1$.

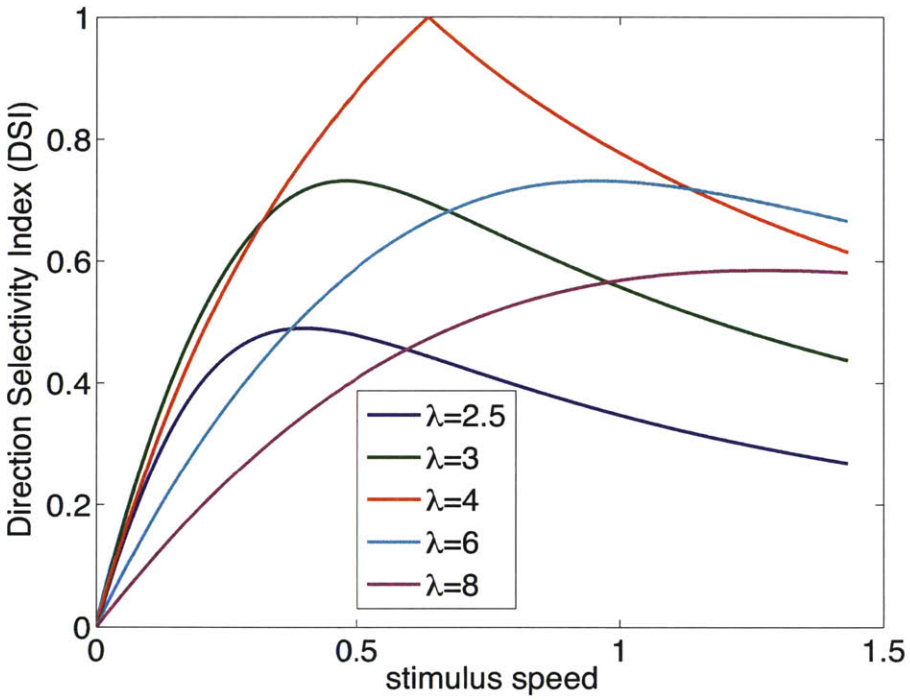

FIGURE 4.5. Model direction selectivity index (DSI) versus stimulus speed.

DSI versus stimulus speed (units of $\Delta x/\tau$) for traveling sine waves of various wavelengths λ (units of Δx). The preferred speed (horizontal location of each peak) is $\lambda/(2\pi)$. Note that responses are cut off at high speeds by the temporal filters of the model, but the DSI can decay more slowly.

4.4. Discussion

In our DS model, SAC dendrites are wired to BC types with different time lags. A previous model did not distinguish between BC types, and instead relied on the time lag of signal conduction within the SAC dendrite itself [Tukker et al., 2004] (Fig. 1.2d). Like most other amacrine cells, SACs lack an axon; their output synapses are found in the distal zones of their dendrites [Famiglietti, 1991] (Fig. 2.3a, inset). Due to dendritic conduction delay, proximal BC inputs should take longer to reach the output synapses than distal BC inputs [Vaney, 1991] (Fig. 1.2d) . Therefore this time lag is also consistent with the empirical finding of an outward preferred direction. To summarize the novelty of our hypothesis, we place the time lag before BC-SAC synapses, whereas the previous model places it after BC-SAC synapses.

The postsynaptic delay model has a major weakness. If dendritic conduction were the only source of time lag, the somatic voltage would exhibit DS with an inward preferred direction, but this is inconsistent with intracellular recordings [Euler et al., 2002] (Fig. 1.2e). In contrast, the presynaptic delay model is compatible with

approximating an SAC dendrite as isopotential (Fig. 1.2c), so preferred direction is predicted to be independent of the location of the voltage measurement, consistent with empirical data [Euler et al., 2002]. It may also be possible to make the postsynaptic delay model consistent with experiments by adding active dendritic conductances [Hausselt et al., 2007].

The presynaptic and postsynaptic delay models are not mutually exclusive. If they work together, passive cable theory suggests that presynaptic delay dominates, because estimated postsynaptic delay is much shorter than the time lag between BC2 and BC3a (Supplementary Equations). Can we gauge the relative importance of the delays empirically rather than theoretically? One way would be intracellular recording at the SAC soma of responses to visual stimulation at various dendritic locations. If postsynaptic delay dominates, then response latency will grow with distance of the visual stimulus from the soma. If presynaptic delay dominates, then distal stimulation will evoke somatic responses with shorter latency than proximal stimulation. This prediction may seem counterintuitive, but is an obvious outcome of our model.

Many other models of DS emergence in SACs invoke inhibition as well as excitation [Borg-Graham and Grzywacz, 1992, Gavrikov et al., 2003, Münch and Werblin, 2006, Lee and Zhou, 2006]. We have focused on excitatory mechanisms, as blocking inhibition does not abolish DS [Euler et al., 2002]. However, inhibition may have the effect of enhancing DS, and its role should be investigated further.

This work focused on Off BC-SAC circuitry. An analogous sustained-transient distinction can also be made for On BC types [Baden et al., 2013, Borghuis et al., 2013]. It remains to be seen whether their connectivity with On SACs depends on distance from the soma. If this turns out to be the case, then the model of Fig. 4.4 could serve as a general theory of motion detection by both On and Off SACs. The model filter of Fig. 4.4a also resembles the spatiotemporal receptive field of the J type of ganglion cell (Fig. 3b of Ref. Kim et al. [2008]).

Neural activity imaging [Maisak et al., 2013] and connectomic analysis [Takemura et al., 2013] have recently identified a plausible candidate for the site of DS emergence in the fly visual system. If our theory is correct, then the analogies between insect and mammalian motion detection [Borst and Euler, 2011] are more far-reaching than previously suspected, with fly T4 and T5 cells corresponding to On and Off SAC dendrites in both connectivity and function.

A glimmer of space-time wiring specificity can even be seen in the structure of the SAC itself. Since BC types with different time lags arborize at different IPL depths, IPL depth can be regarded as a time axis. Therefore, the slight tilt of the SAC dendrites in the IPL (Fig. 4.3a) could be related to the orientation of the SAC receptive field in space-time (Fig. 4.5a). However, dendritic tilt alone is not sufficient to predict our model, as co-stratification sometimes fails to predict contact (Fig. 4.1d, Fig. 5.3b). For example, co-stratification predicts strong BC4 connectivity to distal SAC dendrites. This would favor an inward preferred direction, contrary to what is observed, because BC2 leads (not lags) BC4 in visual responses [Baden et al., 2013].

The idea that contact (or connectivity) can be inferred from co-stratification is sometimes known as Peters' Rule [Braitenberg and Schüz, 1998], and has also been applied to estimate neocortical connectivity [Kalisman et al., 2003, Binzegger et al., 2004, Stepanyants and Chklovskii, 2005]. The present work shows that fairly

subtle violations of Peters' Rule may be important for visual function. Previous research suggests that On-Off direction selective ganglion cells (DSGCs) inherit their DS from SAC inputs due to a strong violation of Peters' Rule [Fried et al., 2002, Yonehara et al., 2010, Wei et al., 2010, Briggman et al., 2011].

Our findings were made possible by using AI to reduce the amount of human effort required for 3D reconstruction of neurons. Even after the labor savings, our research required great human effort from a handful of paid workers in the lab and a large number of volunteers through EyeWire. Our experiences do not support claims that the "wisdom of the crowd" should replace experts [Surowiecki, 2005]. Instead, EyeWire depends on cooperation between lab experts and online amateurs (Methods). Furthermore, some amateurs developed remarkable expertise and were promoted to increasingly sophisticated roles within the EyeWire community (Supplementary Notes). We believe that crowd wisdom requires amplifying the expert voices within the crowd, and also empowering individuals to become experts. Fortunately, such goals are well-matched to the game format.

The EyeWire AI was based on a deep convolutional network [Turaga et al., 2009, 2010]. Similar networks have been successfully applied to serial EM images obtained using conventional staining techniques that mark intracellular organelles [Ciresan et al., 2012]. Extending EyeWire to such images, in which synapses are clearly visible, would enable a true connection analysis that goes beyond the contact and co-stratification analyses employed here.

Our work demonstrates that reconstructing a neural circuit can provide surprising insights into its function. Much more will be learned as reconstruction speed grows. The combination of crowd and artificial intelligence promises a continuous upward path of improvement, as human input from the crowd is not only useful for generating neuroscience discoveries, but also for making the AI more capable through machine learning.

CHAPTER 5

Analagous Connectivity in the On SAC

The starburst amacrine cell (SAC) is a key player in retinal computation of the direction of a moving stimulus. Ablation of SACs impairs the optokinetic reflex, a behavior that depends on computation of visual motion [Yoshida et al., 2001, Amthor et al., 2002]. Both ablation [Yoshida et al., 2001, Amthor et al., 2002] and reversible inactivation [Vlasits et al., 2014] of SACs reduce direction selective (DS) responses in ganglion cells, which receive synaptic input from SACs. SAC dendrites are preferentially activated by visual stimuli that move outward from the soma to the dendritic tips [Euler et al., 2002, Lee and Zhou, 2006, Hausselt et al., 2007].

The proposed mechanisms for DS of SAC dendrites fall into several categories. According to inhibitory cellular hypotheses, dendritic biophysics causes inhibitory input to SACs to have effects that depend on dendritic location [Borg-Graham and Grzywacz, 1992, Gavrikov et al., 2003]. In inhibitory circuit hypotheses, GABAergic synaptic connectivity between SAC dendrites depends on the difference between their preferred directions [Lee and Zhou, 2006, Münch and Werblin, 2006]. In excitatory cellular hypotheses, SAC biophysics causes excitatory input to SACs to have effects that depend on dendritic location [Tukker et al., 2004, Hausselt et al., 2007, Oesch and Taylor, 2010].

Recently we proposed a novel excitatory circuit hypothesis based on specificity of wiring between bipolar cells (BCs) and SACs. The proposal was based on anatomical evidence that sustained and transient BC types are connected to SACs at locations that are near and far from the SAC soma, respectively [Kim et al., 2014]. Such "space-time wiring specificity" could make the BC-SAC circuit function as a correlation-type motion detector [Borst and Euler, 2011], and is consistent with the observed outward preferred direction of SAC dendrites.

Like many other retinal neurons, the SAC comes in both On and Off types. The On SAC resembles a reflection of the Off SAC across a plane through the middle of the inner plexiform layer (IPL) (Fig. 5.1b, d). Probably due to this striking symmetry, DS and its mechanisms are often assumed to be similar between On and Off SACs. This remains merely an assumption as published studies of SACs were typically restricted to a single type. Physiological studies of DS were carried out for On SACs [Euler et al., 2002, Lee and Zhou, 2006, Hausselt et al., 2007], while our anatomical study of BC-SAC wiring specificity was carried out for Off SACs [Kim et al., 2014].

Here we find evidence that the On BC-SAC circuit possesses a space-time wiring specificity analogous to that shown previously for the Off BC-SAC circuit. We reconstructed a large set of On BCs and On SACs from e2198, a dataset of mouse retinal images from serial block-face scanning electron microscopy [Briggman et al., 2011]. Based on the resulting high-resolution information about the anatomy of single cells, we have succeeded in subdividing BC5 into three types that we call

BC5t, BC5i, and BC5o. This finding confirms a speculation of Helmstaedter et al. [2013], who were previously able to distinguish just two BC5 types, but predicted the existence of more. Our definition of a third BC5 type increases the total count of cone BC types to 13.

Contact analysis is consistent with a wiring diagram in which BC7 prefers to synapse closer to the On SAC soma, and BC5 prefers to synapse farther from the soma (Fig. 5.1c). Among the BC5 types, synaptic input from BC5o is likely to be less than from BC5t and BC5i.

Most of the available evidence suggests that transient BC types generally arborize near the IPL center, and sustained BC types near the IPL edges [Baden et al., 2013, Borghuis et al., 2013]. (But see Ichinose et al. 2014 for a divergent view.) Combined with the standard division of the IPL into On and Off sublamina, this yields four sublayers: On-sustained, On-transient, Off-transient, and Off-sustained (Fig. 5.1b). Based on this IPL organization, it is likely that BC7 is sustained and BC5 is transient. If this is the case, then On BC-SAC wiring is analogous to Off BC-SAC wiring.

5.1. BC-SAC contact analysis

We computed contact area between SACs and BCs of each type. The absolute areas were normalized to produce an estimate of the percentage of SAC surface area covered by BCs of each type (Experimental Procedures). This contact analysis suggests that BC5t, BC5i, and BC7 are likely the dominant bipolar cell inputs to the On SAC (Fig. 5.3a, c). Our result is consistent with previous anatomical reconstructions [Helmstaedter et al., 2013] and physiological experiments [Duan et al., 2014, Chen et al., 2014], though these previous studies did not distinguish all three BC5 types. If there is BC5o input, it is likely substantially weaker than BC5t and BC5i input (Fig. 5.3a).

To characterize the spatial relations between contacting cells, we examined the dependence of BC-SAC contact on distance between the BC axon and the SAC soma (Fig. 5.3b). The absolute areas were normalized to estimate the percentage of SAC surface area covered by BCs of a given type at a particular distance from the SAC soma (Experimental Procedures). The resulting graphs show that BC7 prefers to contact On SAC dendrites near the SAC soma, whereas BC5t and BC5i prefer to contact at an intermediate distance from the soma (Fig. 5.3c).

We only reconstructed BCs in the central area of e2198 (Fig. 5.1e), and even within this area some BCs may have been missed (Fig. 3.4e, f, g). In our previous paper, we described methods of analyzing BC-SAC contact that are robust to both kinds of incompleteness [Kim et al., 2014]. The same methods were applied here, with only minor changes.

We compute each SAC's total contact area with all BCs of a given type divided by the SAC's surface area contained in the convex hull of the same BCs. This yields an estimate of the fraction of the SAC's surface in contact with BCs of the given type. This fraction is averaged over SACs to yield the estimates shown in Fig. 5.3A, with standard error based on the number of SACs that intersect the convex hull of the given BC type.

For each BC type, a coverage factor is computed by dividing the sum of hull areas for cells of the given type by the area of the union of hulls of the cells. The

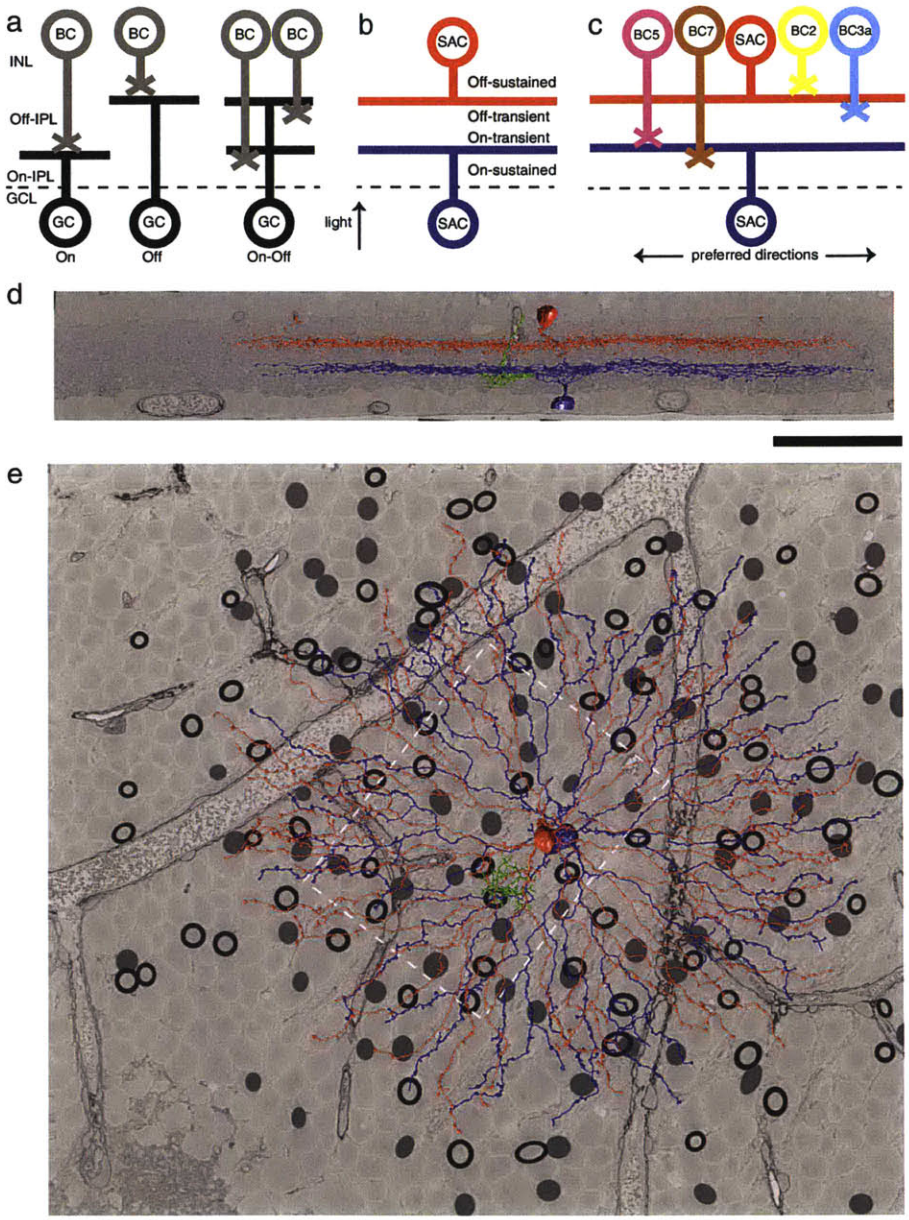

FIGURE 5.1. Organization of the inner plexiform layer
a, The IPL is divided into On and Off (gray shading) sublayers, which support On BC-GC wiring and Off BC-GC wiring specificity. **b**, Observations of BC visual responses [Baden et al., 2013, Borghuis et al., 2013] suggest a division of the IPL into sustained and transient sublayers beyond the on and off division. The two sustained-transient divisions are located at the depths of On and Off starburst amacrine cells (SACs). **c**, Analogous wiring specificity for On and Off BC-SAC circuits. Sustained BCs prefer the proximal zone of SACs and transient BCs prefer the intermediate or distal zones of SACs. **d**, When viewed perpendicular to the light axis, On (blue) and Off (red) SACs appear mirror symmetric across the plane separating the On and Off sublayers of the IPL. **e**, The same SACs appear similar when viewed along the light axis. Black circles and gray dots respectively indicate reconstructed On and Off SAC cell body locations. On BCs were reconstructed in a patch (dashed rectangle). Scale bar, 50 μm.

coverage factor represents the extent to which neighboring BCs of the same type overlap one another.

For each BC-SAC pair, we compute the contact area divided by the surface area of the SAC within the convex hull of the BC. Multiplying by the coverage factor for the BC type yields an estimate of the fraction of the SAC's surface area contacting the BC type at that distance from that SAC's soma. This computation is done for all BC-SAC pairs, except that we discard pairs for which the BC hull contains fewer than 500 SAC surface voxels in order to dampen fluctuations. We bin the remaining BC-SAC pairs by distance and by BC type. For each bin and for each SAC that contributes pairs to that bin, we compute the mean over BC-SAC pairs. Each data point in Fig. 5.3c represents the mean of the SAC-specific means for that bin, and standard error is based on the number of SACs that contribute to that bin.

One might worry that our contact analyses are sensitive to incomplete reconstruction of BCs (see "holes" in the tilings of Fig. 3.4e, f, g). To avoid this problem, the results of our analyses are expressed not as absolute contact areas but instead as fractions of SAC surface area. To demonstrate robustness, we repeated our contact analyses after deleting a random subset of BC5t and BC5i cells (Fig. 5.2a, b, c). The estimates of SAC coverage turned out virtually unchanged (Fig. 5.2d, e); SAC coverage by BC5o was still much lower than by BC5t and BC5i.

The contact analysis was done with BC types given by hierarchical clustering after a small number of swaps to correct for tiling violations, as explained above. The results of the contact analysis look similar if the tiling swaps are not performed (data not shown).

5.2. BC-SAC co-stratification analysis

Fig. 2.5d already showed that proximal SAC dendrites span a wide range of IPL depths, which are different from the depths of the intermediate and distal dendrites. Because of this depth difference, the proximal zone co-stratifies with BC7 but only weakly with BC5, which is consistent with our observed preference of BC7 for contact with the proximal zone. Such reasoning was already used by Famiglietti [1991] to infer that proximal dendrites should receive inputs from different BC types compared to distal dendrites.

This suggests that co-stratification could be used to quantitatively predict On BC-SAC contact using the integral over depth of the product of BC and SAC stratification profiles. Fig. 5.3d shows that this prediction works well in some respects, but not in others. On the one hand, predicted contact (Fig. 5.3d) nicely matches actual contact (Fig. 5.3c) for BC5t, BC5i, and BC7, failing only to match the observed decrease in the distal zone. On the other hand, actual contact of BC6 is much lower than expected from predicted contact.

It may seem surprising that BC6 makes little contact with On SACs, given that it stratifies over a broad range of IPL depths that includes all zones of On SAC dendrites (Fig. 3.4a). One reason may be that the BC6 stratification profile dips down exactly at the depth of intermediate and distal dendrites (Fig. 3.4c), as if BC6 were trying to avoid contacting the On SAC.

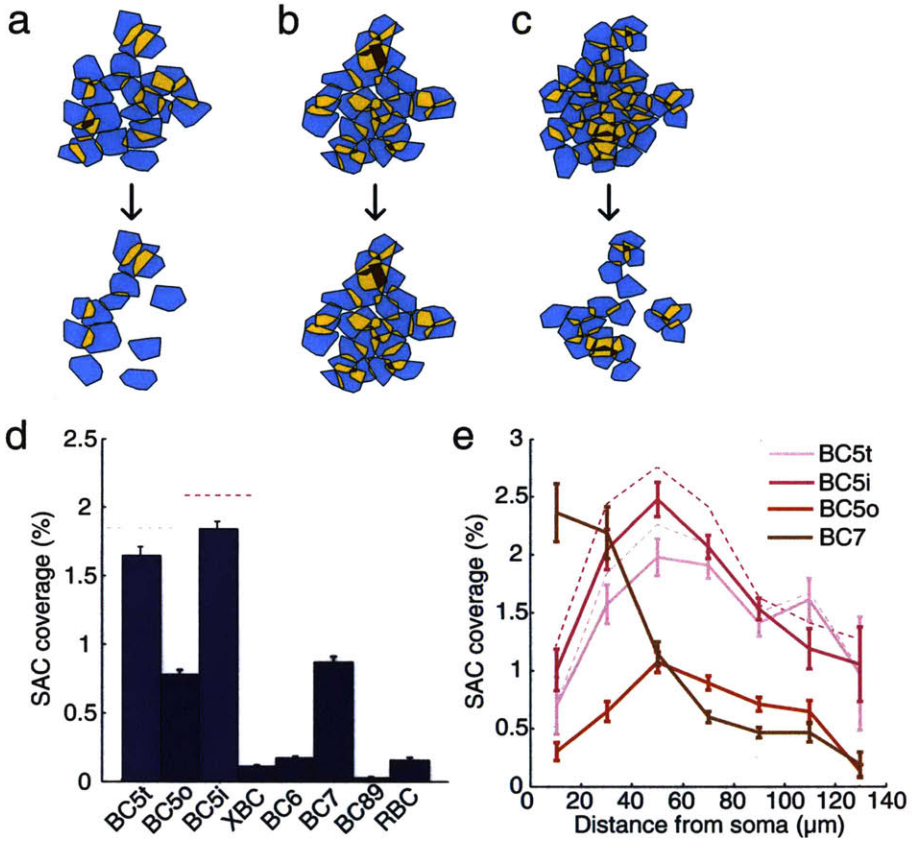

FIGURE 5.2. Robustness of Contact Analysis.
Robustness of contact analysis to missing bipolar cells. Approximately half of BC5i (**a**) and BC5t (**c**) cells were randomly deleted, while BC5o was left unchanged (**b**). The BC5i and BC5t tilings are obviously incomplete, and BC5o now has the most complete coverage. (**d**, **e**) The results of contact analysis (solid lines) are only slightly shifted relative to the original contact analysis of Fig. 5.3**a**, **c** (dashed lines). BC5o still contributes much less than BC5i and BC5t to SAC coverage, even though BC5o cells are now the most numerous.

5.3. Discussion

Our reconstruction of the On BC-SAC circuit suggests that its wiring diagram parallels that of the Off BC-SAC circuit (Fig. 5.1c). We find that sustained BC types prefer to contact SAC dendrites near the SAC soma, and transient BC types prefer an intermediate distance from the SAC soma. We interpret these contact preferences as reflecting synaptic connectivity preferences.

The spatial organization of the IPL has previously been interpreted as supporting rules of wiring specificity. For example, the division of the IPL into On and Off sublayers (Fig. 5.1a) supports On to On and Off to Off rules for wiring of BCs

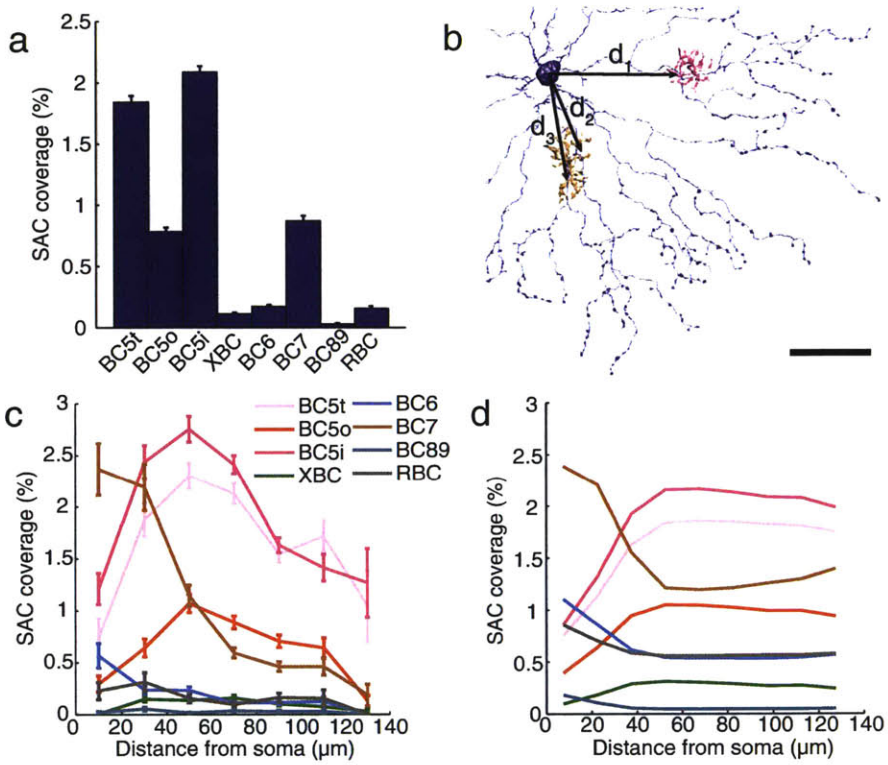

FIGURE 5.3. Wiring specificity of On BC-SAC circuit.
a, Fraction of On SAC surface area contacted by On BC types. **b**, Distance is defined for each BC-SAC pair in the tangential plane from the centroid of BC-SAC contact to the point on the SAC soma from which the dendritic trunk emerges. The centroid of emergence points is used if there are multiple trunks. **c**, Fraction of On SAC surface contacted by On BC types versus distance from the SAC soma. Standard error is based on the number of pairs for each BC type and distance. **d**, Contact predicted from co-stratification analysis. Scale bar, 30 μm.

to ganglion cells (GCs) [Famiglietti and Kolb, 1976a, Pang et al., 2003]. Similarly, the division of the IPL into sustained and transient sublayers (Fig. 5.1b) could support sustained to sustained and transient to transient rules of BC-GC wiring [Awatramani and Slaughter, 2000]. Here the BC-SAC wiring diagram provides an explanation of why On and Off SACs are located at the boundaries between sustained and transient IPL sublayers (Fig. 5.1b). Namely, this positioning is appropriate for receiving convergent input from both sustained and transient BC types (Fig. 5.1c).

We also find three differences between the On and Off circuits. First, BC7 and BC5i/t prefer to contact closer to the On SAC soma than their analogs BC2 and BC3a contact to the Off SAC soma (compare Fig. 5.3c with Fig. 4.1d). Second, the On SAC is contacted strongly by two transient BC types, while the Off SAC

receives strong contact from a single transient BC type. Third, BC contact on distal SAC dendrites is relatively scarcer for the On than the Off circuit (Fig. 2.3).

The current study comes with several caveats. First, while most of the available evidence supports the sustained-transient classification of On BC types adopted in this paper [Baden et al., 2013, Borghuis et al., 2013], the literature contains at least one divergent report about this classification [Ichinose et al., 2014]. Second, synaptic connectivity cannot be identified with certainty in e2198, because of an unconventional staining technique that left intracellular organelles invisible. Therefore we rely on contact between cells as an indirect indicator of connectivity. Third, motion computation by SAC dendrites might involve biophysics of SAC dendrites [Gavrikov et al., 2003, Tukker et al., 2004, Hausselt et al., 2007], which is not incompatible with our hypothetical mechanism involving space-time wiring specificity.

We were able to divide BC5 into three types (BC5t, BC5o, and BC5i), based on differences in stratification. Using patterns of contact with two ganglion cell types, we also replicated the prior two-way division by Helmstaedter et al. [2013] of BC5 into BC5A and BC5R, and found that BC5A corresponds almost perfectly with BC5i. We were able to assign all BC5 cells to either BC5A and BC5R, because our reconstructions of the ganglion cell types are more complete than those of Helmstaedter et al. [2013]. In the future, we expect contact or connectivity to replace stratification as the main property used to classify cells into types [Seung, 2009, 2012, Jonas and Kording, 2015].

Wässle et al. [2009] defined BC5 using a 5-HT3R-EGFP transgenic mouse line. They speculated that the line labeled two BC5 types, because of the high density of labeled cells, and because two BC5 types had been molecularly distinguished in rat [Fyk-Kolodziej and Pourcho, 2007]. However, they were unable to find molecular markers distinguishing BC5 types in mouse. Duan et al. [2014] showed that Kcng4 and Cdh9 Cre lines label the same cells as 5-HT3R-EGFP. Haverkamp et al. [2009] found that the BC5 cells in the 5-HT3R-EGFP line were all CaBP5-positive. BC5t may be CaBP5-negative (Haruhisa Okawa and Rachel Wong, private communication). If this is the case, it follows that BC5o and BC5i correspond to the two types in the 5-HT3R-EGFP transgenic line.

The catalog of mouse BC types is likely complete. Our claim is based on two assumptions: (1) every BC type tiles the retina with little overlap, and (2) there are no large BCs, which would be rare and therefore could have been missed by our reconstructions and those of Helmstaedter et al. [2013]. One anomaly is that BC1 and BC2 tilings exhibit more overlap than those of other types (Extended Data Figure 6 of Kim et al. 2014). The overlap is not enough to allow defining a third type that fully tiles the retina; a hypothetical third type would be sparse in its coverage. Another qualification is that our reconstructions come from a single location in a retina, so we cannot exclude the possibility that cell types vary across the retina.

-

Bibliography

E H Adelson and J R Bergen. Spatiotemporal energy models for the perception of motion. *J Opt Soc Am A*, 2(2):284–99, Feb 1985.

Franklin R Amthor, Keyser Kent T, and Nina A Dmitrieva. Effects of the destruction of starburst-cholinergic amacrine cells by the toxin af64a on rabbit retinal directional selectivity. *Visual neuroscience*, 19(04):495–509, 2002.

G B Awatramani and M M Slaughter. Origin of transient and sustained responses in ganglion cells of the retina. *J Neurosci*, 20(18):7087–95, Sep 2000.

Stephen A Baccus and Markus Meister. Fast and slow contrast adaptation in retinal circuitry. *Neuron*, 36(5):909–19, Dec 2002.

Tom Baden, Philipp Berens, Matthias Bethge, and Thomas Euler. Spikes in mammalian bipolar cells support temporal layering of the inner retina. *Curr Biol*, 23 (1):48–52, 2013.

H B Barlow and W R Levick. The mechanism of directionally selective units in rabbit's retina. *J Physiol*, 178(3):477–504, Jun 1965.

H B Barlow, R M Hill, and W R Levick. Retinal ganglion cells responding selectively to direction and speed of image motion in the rabbit. *J Physiol*, 173:377–407, Oct 1964.

Horace B Barlow and Richard M Hill. Selective sensitivity to direction of movement in ganglion cells of the rabbit retina. *Science*, 139(3553):412–412, 1963.

M J Berry, II and M Meister. Refractoriness and neural precision. *J Neurosci*, 18 (6):2200–11, Mar 1998.

Tom Binzegger, Rodney J Douglas, and Kevan A C Martin. A quantitative map of the circuit of cat primary visual cortex. *J Neurosci*, 24(39):8441–53, Sep 2004. doi: 10.1523/JNEUROSCI.1400-04.2004.

Lyle J Borg-Graham and Norberto M Grzywacz. A model of the directional selectivity circuit in retina: transformations by neurons singly and in concert. In *Single neuron computation*, chapter 13, pages 347–76. Academic San Diego, 1992.

Bart G Borghuis, Jonathan S Marvin, Loren L Looger, and Jonathan B Demb. Two-photon imaging of nonlinear glutamate release dynamics at bipolar cell synapses in the mouse retina. *J Neurosci*, 33(27):10972–85, 2013.

Alexander Borst and Thomas Euler. Seeing things in motion: models, circuits, and mechanisms. *Neuron*, 71(6):974–94, Sep 2011. doi: 10.1016/j.neuron.2011.08.031.

Alexander Borst, Carolina Reisenman, and Juergen Haag. Adaptation of response transients in fly motion vision. II: Model studies. *Vision Res*, 43(11):1309–22, May 2003.

Valentino Braitenberg and Almut Schüz. *Cortex: statistics and geometry of neuronal connectivity*. Springer Berlin, 2nd edition edition, 1998.

Kevin L Briggman, Moritz Helmstaedter, and Winfried Denk. Wiring specificity in the direction-selectivity circuit of the retina. *Nature*, 471(7337):183–8, Mar 2011.

doi: 10.1038/nature09818.

Minggang Chen, Seunghoon Lee, Silvia J H Park, Loren L Looger, and Z Jimmy Zhou. Receptive field properties of bipolar cell axon terminals in direction-selective sublaminas of the mouse retina. *J Neurophysiol*, 112(8):1950–62, Oct 2014. doi: 10.1152/jn.00283.2014.

Dan Ciresan, Alessandro Giusti, Juergen Schmidhuber, et al. Deep neural networks segment neuronal membranes in electron microscopy images. In *Advances in Neural Information Processing Systems 25*, pages 2852–2860, 2012.

Seth Cooper, Firas Khatib, Adrien Treuille, Janos Barbero, Jeehyung Lee, Michael Beenen, Andrew Leaver-Fay, David Baker, Zoran Popović, and Foldit Players. Predicting protein structures with a multiplayer online game. *Nature*, 466(7307): 756–60, Aug 2010. doi: 10.1038/nature09304.

JE Dowling and BB Boycott. Organization of the primate retina: electron microscopy. *Proceedings of the Royal Society of London B: Biological Sciences*, 166 (1002):80–111, 1966.

Xin Duan, Arjun Krishnaswamy, Irina De la Huerta, and Joshua R Sanes. Type ii cadherins guide assembly of a direction-selective retinal circuit. *Cell*, 158(4): 793–807, Aug 2014. doi: 10.1016/j.cell.2014.06.047.

Thomas Euler, Peter B Detwiler, and Winfried Denk. Directionally selective calcium signals in dendrites of starburst amacrine cells. *Nature*, 418(6900):845–52, 2002.

E V Famiglietti. Synaptic organization of starburst amacrine cells in rabbit retina: analysis of serial thin sections by electron microscopy and graphic reconstruction. *J Comp Neurol*, 309(1):40–70, Jul 1991. doi: 10.1002/cne.903090105.

E V Famiglietti, Jr. On and off pathways through amacrine cells in mammalian retina: the synaptic connections of "starburst" amacrine cells. *Vision Res*, 23 (11):1265–79, 1983.

E V Famiglietti, Jr and H Kolb. Structural basis for on-and off-center responses in retinal ganglion cells. *Science*, 194(4261):193–5, Oct 1976a.

Edward V Famiglietti. Functional architecture of cone bipolar cells in mammalian retina. *Vision research*, 21(11):1559–1563, 1981.

EV Famiglietti and Helga Kolb. Structural basis for on-and off-center responses in retinal ganglion cells. *Science*, 194(4261):193–195, 1976b.

EV Famiglietti, Akimichi Kaneko, and Masao Tachibana. Neuronal architecture of on and off pathways to ganglion cells in carp retina. *Science*, 198(4323):1267–1269, 1977.

J C Fiala. Reconstruct: a free editor for serial section microscopy. *J Microsc*, 218 (Pt 1):52–61, Apr 2005. doi: 10.1111/j.1365-2818.2005.01466.x.

Shelley I Fried, Thomas A Münch, and Frank S Werblin. Mechanisms and circuitry underlying directional selectivity in the retina. *Nature*, 420(6914):411–4, Nov 2002. doi: 10.1038/nature01179.

Bozena Fyk-Kolodziej and Roberta G Pourcho. Differential distribution of hyperpolarization-activated and cyclic nucleotide-gated channels in cone bipolar cells of the rat retina. *Journal of Comparative Neurology*, 501(6):891–903, 2007.

Konstantin E Gavrikov, Andrey V Dmitriev, Kent T Keyser, and Stuart C Mangel. Cation–chloride cotransporters mediate neural computation in the retina. *Proc Natl Acad Sci U S A*, 100(26):16047–52, Dec 2003. doi: 10.1073/pnas.2637041100.

Krishna K Ghosh, Sascha Bujan, Silke Haverkamp, Andreas Feigenspan, and Heinz Wässle. Types of bipolar cells in the mouse retina. *J Comp Neurol*, 469(1):70–82, Jan 2004. doi: 10.1002/cne.10985.

Susanne E Hausselt, Thomas Euler, Peter B Detwiler, and Winfried Denk. A dendrite-autonomous mechanism for direction selectivity in retinal starburst amacrine cells. *PLoS Biol.*, 5(7):e185, 2007.

S Haverkamp, D Inta, H Monyer, and H Wässle. Expression analysis of green fluorescent protein in retinal neurons of four transgenic mouse lines. *Neuroscience*, 160(1):126–139, 2009.

Moritz Helmstaedter, Kevin L Briggman, Srinivas C Turaga, Viren Jain, H Sebastian Seung, and Winfried Denk. Connectomic reconstruction of the inner plexiform layer in the mouse retina. *Nature*, 500(7461):168–74, Aug 2013. doi: 10.1038/nature12346.

Tomomi Ichinose, Bozena Fyk-Kolodziej, and Jesse Cohn. Roles of on cone bipolar cell subtypes in temporal coding in the mouse retina. *J Neurosci*, 34(26):8761–71, Jun 2014. doi: 10.1523/JNEUROSCI.3965-13.2014.

Chang-Jin Jeon, Enrica Strettoi, and Richard H. Masland. The major cell populations of the mouse retina. *J Neurosci*, 18(21):8936–8946, Aug 1998.

Eric Jonas and Konrad Kording. Automatic discovery of cell types and microcircuitry from neural connectomics. *eLife*, 4:e04250, 2015.

Nir Kalisman, Gilad Silberberg, and Henry Markram. Deriving physical connectivity from neuronal morphology. *Biol Cybern*, 88(3):210–8, Mar 2003. doi: 10.1007/s00422-002-0377-3.

Akimichi Kaneko. Physiological and morphological identification of horizontal, bipolar and amacrine cells in goldfish retina. *The Journal of physiology*, 207 (3):623–633, 1970.

In-Jung Kim, Yifeng Zhang, Masahito Yamagata, Markus Meister, and Joshua R Sanes. Molecular identification of a retinal cell type that responds to upward motion. *Nature*, 452(7186):478–82, Mar 2008. doi: 10.1038/nature06739.

Jinseop S Kim, Matthew J Greene, Aleksandar Zlateski, Kisuk Lee, Mark Richardson, Srinivas C Turaga, Michael Purcaro, Matthew Balkam, Amy Robinson, Bardia F Behabadi, Michael Campos, Winfried Denk, H Sebastian Seung, and the EyeWirers. Space-time wiring specificity supports direction selectivity in the retina. *Nature*, 509(7500):331–6, May 2014. doi: 10.1038/nature13240.

L Lagnado, A Gomis, and C Job. Continuous vesicle cycling in the synaptic terminal of retinal bipolar cells. *Neuron*, 17(5):957–67, Nov 1996.

Seunghoon Lee and Z Jimmy Zhou. The synaptic mechanism of direction selectivity in distal processes of starburst amacrine cells. *Neuron*, 51(6):787–99, Sep 2006. doi: 10.1016/j.neuron.2006.08.007.

Jerome Y Lettvin, Humberto R Maturana, Warren S McCulloch, and Walter H Pitts. What the frog's eye tells the frog's brain. *Proceedings of the IRE*, 47(11): 1940–1951, 1959.

C.J. Lintott, K. Schawinski, A. Slosar, K. Land, S. Bamford, D. Thomas, M.J. Raddick, R.C. Nichol, A. Szalay, D. Andreescu, et al. Galaxy Zoo: morphologies derived from visual inspection of galaxies from the Sloan Digital Sky Survey. *Monthly Notices of the Royal Astronomical Society*, 389(3):1179–1189, 2008.

Matthew S Maisak, Juergen Haag, Georg Ammer, Etienne Serbe, Matthias Meier, Aljoscha Leonhardt, Tabea Schilling, Armin Bahl, Gerald M Rubin, Aljoscha

Nern, Barry J Dickson, Dierk F Reiff, Elisabeth Hopp, and Alexander Borst. A directional tuning map of drosophila elementary motion detectors. *Nature*, 500 (7461):212–6, Aug 2013. doi: 10.1038/nature12320.

Michael B Manookin, Deborah Langrill Beaudoin, Zachary Raymond Ernst, Leigh J Flagel, and Jonathan B Demb. Disinhibition combines with excitation to extend the operating range of the off visual pathway in daylight. *J Neurosci*, 28(16): 4136–50, Apr 2008. doi: 10.1523/JNEUROSCI.4274-07.2008.

Richard H Masland. Neuronal cell types. *Current Biology*, 14(13):R497–R500, 2004.

Stephen L Mills and Stephen C Massey. Morphology of bipolar cells labeled by dapi in the rabbit retina. *Journal of Comparative Neurology*, 321(1):133–149, 1992.

L Missotten. The synapses in the human retina. In *The structure of the eye*, volume 2, pages 17–28. Schattauer-Verlag Stuttgart, 1965.

Thomas A Münch and Frank S Werblin. Symmetric interactions within a homogeneous starburst cell network can lead to robust asymmetries in dendrites of starburst amacrine cells. *J Neurophysiol*, 96(1):471–7, Jul 2006. doi: 10.1152/jn.00628.2005.

R Nelson, EV Famiglietti, and H Kolb. Intracellular staining reveals different levels of stratification for on-and off-center ganglion cells in cat retina. *Journal of Neurophysiology*, 41(2):472–483, 1978.

Nicholas W Oesch and W Rowland Taylor. Tetrodotoxin-resistant sodium channels contribute to directional responses in starburst amacrine cells. *PLoS One*, 5(8): e12447, 2010. doi: 10.1371/journal.pone.0012447.

Ji-Jie Pang, Fan Gao, and Samuel M Wu. Light-evoked excitatory and inhibitory synaptic inputs to on and off α ganglion cells in the mouse retina. *The Journal of neuroscience*, 23(14):6063–6073, 2003.

Wilfrid Rall. Theoretical significance of dendritic trees for neuronal input-output relations. In R. F. Reis, editor, *Neural theory and modeling*, pages 73–97. Stanford Univ. Press, 1964.

Werner Reichardt. Autocorrelation, a principle for the evaluation of sensory information by the central nervous system. In *Sensory communication*, pages 303–317. 1961.

H Sebastian Seung. Reading the book of memory: sparse sampling versus dense mapping of connectomes. *Neuron*, 62(1):17–29, 2009.

H Sebastian Seung and Uygar Sümbül. Neuronal cell types and connectivity: lessons from the retina. *Neuron*, 83(6):1262–72, Sep 2014. doi: 10.1016/j.neuron.2014.08.054.

Sebastian Seung. *Connectome: How the brain's wiring makes us who we are*. Houghton Mifflin Harcourt, 2012.

Sandra Siegert, Brigitte Gross Scherf, Karina Del Punta, Nick Didkovsky, Nathaniel Heintz, and Botond Roska. Genetic address book for retinal cell types. *Nat Neurosci*, 12(9):1197–204, Sep 2009. doi: 10.1038/nn.2370.

Armen Stepanyants and Dmitri B Chklovskii. Neurogeometry and potential synaptic connectivity. *Trends Neurosci*, 28(7):387–94, Jul 2005. doi: 10.1016/j.tins.2005.05.006.

Uygar Sümbül, Sen Song, Kyle McCulloch, Michael Becker, Bin Lin, Joshua R Sanes, Richard H Masland, and H Sebastian Seung. A genetic and computational approach to structurally classify neuronal types. *Nat Commun*, 5:3512, 2014. doi: 10.1038/ncomms4512.

James Surowiecki. *The Wisdom of Crowds*. Anchor, 2005.

Shin-ya Takemura, Arjun Bharioke, Zhiyuan Lu, Aljoscha Nern, Shiv Vitaladevuni, Patricia K Rivlin, William T Katz, Donald J Olbris, Stephen M Plaza, Philip Winston, Ting Zhao, Jane Anne Horne, Richard D Fetter, Satoko Takemura, Katerina Blazek, Lei-Ann Chang, Omotara Ogundeyi, Mathew A Saunders, Victor Shapiro, Christopher Sigmund, Gerald M Rubin, Louis K Scheffer, Ian A Meinertzhagen, and Dmitri B Chklovskii. A visual motion detection circuit suggested by Drosophila connectomics. *Nature*, 500(7461):175–81, Aug 2013. doi: 10.1038/nature12450.

John J Tukker, W Rowland Taylor, and Robert G Smith. Direction selectivity in a model of the starburst amacrine cell. *Visual neuroscience*, 21(4):611–625, 2004.

Srinivas Turaga, Kevin Briggman, Moritz Helmstaedter, Winfried Denk, and Sebastian Seung. Maximin affinity learning of image segmentation. In Y. Bengio, D. Schuurmans, J. Lafferty, C. K. I. Williams, and A. Culotta, editors, *Advances in Neural Information Processing Systems 22*, pages 1865–1873. 2009.

Srinivas C Turaga, Joseph F Murray, Viren Jain, Fabian Roth, Moritz Helmstaedter, Kevin Briggman, Winfried Denk, and H Sebastian Seung. Convolutional networks can learn to generate affinity graphs for image segmentation. *Neural Comput*, 22(2):511–38, Feb 2010. doi: 10.1162/neco.2009.10-08-881.

David I Vaney. Many diverse types of retinal neurons show tracer coupling when injected with biocytin or neurobiotin. *Neuroscience letters*, 125(2):187–190, 1991.

David I Vaney, Benjamin Sivyer, and W Rowland Taylor. Direction selectivity in the retina: symmetry and asymmetry in structure and function. *Nat. Rev. Neurosci*, 13(3):194–208, Mar 2012. doi: 10.1038/nrn3165.

Anna L Vlasits, Rémi Bos, Ryan D Morrie, Cécile Fortuny, John G Flannery, Marla B Feller, and Michal Rivlin-Etzion. Visual stimulation switches the polarity of excitatory input to starburst amacrine cells. *Neuron*, 83(5):1172–84, Sep 2014. doi: 10.1016/j.neuron.2014.07.037.

Luis Von Ahn and Laura Dabbish. Labeling images with a computer game. In *Proceedings of the SIGCHI conference on human factors in computing systems*, pages 319–326. ACM, 2004.

H. Wässle, C. Puller, F. Müller, and S. Haverkamp. Cone contacts, mosaics, and territories of bipolar cells in the mouse retina. *The Journal of Neuroscience*, 29 (1):106–117, 2009.

A B Watson and A J Ahumada, Jr. Model of human visual-motion sensing. *J Opt Soc Am A*, 2(2):322–41, Feb 1985.

Wei Wei, Aaron M Hamby, Kaili Zhou, and Marla B Feller. Development of asymmetric inhibition underlying direction selectivity in the retina. *Nature*, 469(7330): 402–406, 2010.

FRANK S Werblin and JOHN E Dowling. Organization of the retina of the mudpuppy, necturus maculosus. ii. intracellular recording. *Journal of neurophysiology*, 32(3):339–355, 1969.

Roger W West. Bipolar and horizontal cells of the gray squirrel retina: Golgi morphology and receptor connections. *Vision Research*, 18(2):129–136, 1978.

J G White, E Southgate, J N Thomson, and S Brenner. The structure of the nervous system of the nematode caenorhabditis elegans. *Philos Trans R Soc Lond B Biol Sci*, 314(1165):1–340, Nov 1986.

TN Wiesel. Receptive fields of ganglion cells in the cat's retina. *The Journal of physiology*, 153(3):583–594, 1960.

ML Wolbarsht, HG Wagner, and EF MacNichol Jr. Receptive fields of retinal ganglion cells: extent and spectral sensitivity. In *Neurophysiologie und Psychophysik des Visuellen Systems/The Visual System: Neurophysiology and Psychophysics*, pages 170–177. Springer, 1961.

Harry J Wyatt and Nigel W Daw. Directionally sensitive ganglion cells in the rabbit retina: specificity for stimulus direction, size, and speed. *Journal of Neurophysiology*, 38(3):613–626, 1975.

Keisuke Yonehara, Kamill Balint, Masaharu Noda, Georg Nagel, Ernst Bamberg, and Botond Roska. Spatially asymmetric reorganization of inhibition establishes a motion-sensitive circuit. *Nature*, 469(7330):407–410, 2010.

Keisuke Yonehara, Karl Farrow, Alexander Ghanem, Daniel Hillier, Kamill Balint, Miguel Teixeira, Josephine Jüttner, Masaharu Noda, Rachael L Neve, Karl-Klaus Conzelmann, and Botond Roska. The first stage of cardinal direction selectivity is localized to the dendrites of retinal ganglion cells. *Neuron*, 79(6):1078–85, Sep 2013. doi: 10.1016/j.neuron.2013.08.005.

K Yoshida, D Watanabe, H Ishikane, M Tachibana, I Pastan, and S Nakanishi. A key role of starburst amacrine cells in originating retinal directional selectivity and optokinetic eye movement. *Neuron*, 30(3):771–80, Jun 2001.

Z Jimmy Zhou and Seunghoon Lee. Synaptic physiology of direction selectivity in the retina. *J Physiol*, 586(Pt 18):4371–6, Sep 2008. doi: 10.1113/jphysiol.2008.159020.